

Accepted Article

Groundwater affects the geomorphic and hydrologic properties of coevolved landscapes

David G. Litwin¹, Gregory E. Tucker^{2,3}, Katherine R. Barnhart^{2,3,4}, Ciaran J. Harman^{1,5}

¹Department of Environmental Health and Engineering, Johns Hopkins University, Baltimore, MD, USA
²Cooperative Institute for Research in Environmental Sciences (CIRES), University of Colorado, Boulder,

CO, USA

³Department of Geological Sciences, University of Colorado, Boulder, CO, USA

⁴Now at U.S. Geological Survey, Landslide Hazards Program, Golden, CO, USA

¹Department of Earth and Planetary Science, Johns Hopkins University, Baltimore, MD, USA

Key Points:

- Presents a coupled model of shallow groundwater and landscape evolution to examine coevolution of runoff generation and landscape morphology
- Analysis of the model suggest that hillslope length scales nonlinearly with subsurface drainage capacity relative to the recharge rate
- Emergent morphology can be characterized by 3 metrics (steepness, curvature, topographic index) and is controlled by 4 dimensionless numbers

Corresponding author: Ciaran J. Harman, charman1@jhu.edu

This article has been accepted for publication and undergone full peer review but has not been through the copyediting, typesetting, pagination and proofreading process, which may lead to differences between this version and the Version of Record. Please cite this article as doi: 10.1029/2021JF006239.

This article is protected by copyright. All rights reserved.

Abstract

The hydrologic dynamics and geomorphic evolution of watersheds are intimately coupled – runoff generation and water storage are controlled by topography and properties of the surface and subsurface, while also affecting the evolution of those properties over geologic time. However, the large disparity between their timescales has made it difficult to examine interdependent controls on emergent hydro-geomorphic properties, such as hillslope length, drainage density, extent of surface saturation. In this study, we develop a new model coupling hydrology and landscape evolution to explore how runoff generation affects long-term catchment evolution, and analyze numerical results using a nondimensional scaling framework. We focus on hydrologic processes dominating in humid climates where storm runoff primarily arises from shallow subsurface flow and from precipitation on saturated areas. The model solves hydraulic groundwater equations to predict the water-table location given prescribed, constant groundwater recharge. Water in excess of the subsurface capacity for transport becomes overland flow, which generates shear stress on the surface and may detach and transport sediment. This affects the landscape form that in turn affects runoff generation. We show that (1) four dimensionless parameters describe the possible steady-state landscapes that coevolve under steady recharge; (2) hillslope length increases with increasing transmissivity relative to the recharge rate; (3) three topographic metrics—steepness index, Laplacian curvature, and topographic index—together provide a basis for interpreting landscapes that have coevolved with runoff generated via shallow subsurface flow. Finally we discuss the possibilities and limitations for quantitative comparisons between the model results and real landscapes.

Plain Language Summary

Watersheds store and release water in response to precipitation in complex ways. Much of our understanding of how this happens is linked with the form of the landscape: its topography, soils, and underlying rock. However, over long timescales (thousands to millions of years), the flow of water plays a critical role in shaping these landscape properties through processes like erosion and subsurface weathering. Consequently, we expect many places have key links between their topographic form and hydrological properties. We present a new model to explore these effects, focusing on the feedbacks between surface erosion and runoff generation from seepage of shallow groundwater and precipitation on saturated areas. Runoff can detach sediment, changing the topography. Topographic slope is in turn a driving force of groundwater flow. By grouping the model parameters together, we develop a set of knobs that we can turn to explore the model output. We find that when the subsurface has greater capacity to transmit water (relative to the precipitation supplied), the spacing between stream channels is greater. The results illuminate key topographic properties of landscapes that evolve with shallow groundwater, though much work remains before we can adequately compare results from this type of model with data.

1 Introduction**1.1 Motivation**

Landscape morphology and subsurface structure are strong predictors of runoff generation style and spatial distribution (Dunne, 1978). In humid climates, the infiltration capacity of undisturbed soil is high and overland flow due to exceedance of soil infiltration capacity is rare. When relief is relatively low and soils are relatively thin, runoff is most commonly generated by the expansion of variable source areas, which may generate overland flow where precipitation falls directly on saturated areas (Dunne & Black, 1970). In steeper landscapes with deep soils, water may be transmitted laterally through the subsurface at permeability contrasts, becoming surface runoff only when it reaches stream channels (Hewlett & Hibbert, 1967). Saturated areas (including wetted stream

channels) emerge as the supply of water from upslope areas exceeds the conveyance capacity of water through the subsurface. This competition between upslope supply and downslope transport capacity links properties of the subsurface, such as transmissivity, to the runoff response of watersheds as a whole (O'Loughlin, 1981). Furthermore, overland flow generates shear stress on the land surface that may detach and transport sediment. This drives the evolution of topographic convergence/divergence and convexity/concavity, which are important controls on runoff generation themselves (Prancevic & Kirchner, 2019; Troch et al., 2003; Lepides et al., 2020). Research also suggests that incision and hillslope sediment transport play a role in setting the rate and extent of subsurface weathering by setting the rate at which fresh bedrock is supplied to the near surface (Gabet & Mudd, 2009; West et al., 2005). Weathering is in turn crucial for setting subsurface properties including porosity and hydraulic conductivity that affect groundwater flow and storage capacity.

These feedbacks further suggest that there should be intimate links between runoff generation behavior and landscape morphology (Jefferson et al., 2010; Yoshida & Troch, 2016; Manga, 1996). The long timescales of geomorphic evolution limit our ability to study these relationships directly. An alternative approach is to examine signatures of these processes in observable landscape morphology. Topographic metrics including drainage density, channel steepness, curvature, and topographic (wetness) index have been essential in understanding hydrologic and geomorphic processes in the past. However, it is unclear how these metrics might encode aspects of the coevolution of landscape morphology and hydrological processes. If morphology affects and is affected by runoff generation, how might long-term evolution affect emergent topographic properties and the extent of surface saturation in a landscape? Here we will draw insights from a coupled hydrogeomorphic model in which we can examine the emergent features of landscapes evolved with known subsurface properties and runoff generation mechanisms.

1.2 How has runoff generation been represented in landscape evolution models?

Over geologic time, upland landscapes are shaped by the competition between incision by overland flow, gravitationally-driven fluxes of sediment due to processes including biogenic disturbance and frost heaving, and baselevel change (Howard, 1994). While it is not possible to observe the evolution of landscapes at human timescales, numerical landscape evolution models (LEMs) have allowed researchers to make substantial progress in understanding how landscapes respond to dynamic forcings of tectonics, lithology, and climate (e.g., reviews by Chen et al., 2014; Bishop, 2007; Martin & Church, 2004; Pelletier, 2013; Pazzaglia, 2003; Temme et al., 2013; Valters, 2016). However, the treatment of hydrology in models that consider evolution over geologic time remains rudimentary.

Early LEMs treated runoff as the product of upslope area and an effective precipitation rate (Willgoose, Bras, & RodriguezIturbe, 1991; Ahnert, 1976; Armstrong, 1976), representing the time-averaged runoff from infiltration excess overland flow. In these models, all areas of the landscape generated surface runoff simultaneously, though all areas might not experience erosion due to the presence of thresholds for sediment detachment (Horton, 1945). The practice of using such runoff formulations in LEMs is still common today when hydrologic response is not central to the study, as models with minimal hydrologic dynamics can still effectively capture certain essential aspects of landscape form (e.g., Forte et al., 2016; Barnhart, Tucker, Doty, Glade, et al., 2020; Theodoratos et al., 2018). One of the first attempts to capture subsurface hydrology in a LEM was the model developed by Ijsssz-Vsquez et al. (1992), in which precipitation was partitioned between surface and subsurface flow using a steady-state topographic index criterion (Beven & Kirkby, 1979). The authors found that this partitioning significantly changed catchment hypsometry in comparison to the infiltration excess formulation. Tucker and Bras (1998) compared several different landscape evolution and runoff generation formulations, in-

cluding one that treated subsurface transport capacity similarly to Ijssz-Vsquez et al. (1992). They found that the evolved landscapes have sharp hillslope-valley transitions at a critical value of topographic index. These transitions were smoothed by treating precipitation as a random process with an exponential distribution, rather than having a single value. However, the topographic index type models neglect the role of nonlinearities in groundwater flow, and antecedent conditions that determine catchment runoff response to precipitation. We refer to flow nonlinearity as the degree to which groundwater flow is driven by diffusion due to gradients in aquifer thickness rather than kinematic wave motion in which flow is driven by the slope of permeability contrasts, which can have significant effects on runoff generation (Harman & Sivapalan, 2009). The steady-state assumption of the topographic index model assumes that a storm event is effectively independent of prior events, and arrives with the full subsurface capacity available to drain flow. Many hydrological studies have shown that antecedent conditions are important controls on runoff magnitudes, where wetter systems are primed for larger runoff response due to lack of available subsurface storage or transport capacity (Brocca et al., 2009; Tramblay et al., 2010).

Several studies have coupled landscape evolution with hydrological processes in greater detail. Huang and Niemann (2006, 2008) developed a coupled groundwater model and LEM, and demonstrated the importance of dynamic runoff generation mechanisms for the topographic evolution of different areas of modeled basins. Huang and Niemann (2006) focused on the evolution of a single well-studied catchment, and found that as they simulated its evolution from present, runoff was increasingly generated by subsurface lateral flow rather than saturation excess overland flow. Huang and Niemann (2008) explored the long-term geomorphic evolution of synthetic catchments with groundwater flow, and concluded that the hypsometry of steady-state landscapes was not generally distinguishable between surface-water-dominated and groundwater-dominated landscapes. However, sensitivity of modeled topography to parameters was conducted by imposing changes directly onto the slope-area relationship, rather than examining results of the coupled model, making it more difficult to evaluate the precise role of groundwater flow in long term evolution. Zhang et al. (2016) presented a highly detailed, coupled hydrological model and LEM, though to our knowledge it has not been used beyond the initial proof of concept. With solutions to Richards equation for subsurface flow and St. Venant's equation for surface flow and employment of several dozen parameters, this model is computationally expensive and may be more complex than needed to explore process feedbacks between shallow subsurface hydrology and landscape evolution. A systematic approach is needed to understand these feedbacks. It must be simple enough for interpretation of process controls while still having the core elements of landscape evolution and dynamic runoff generation from the shallow subsurface.

1.3 Scaling and dimensionless landscape morphology

The generation of surface runoff can be seen as the failure of the subsurface to drain precipitation inputs. The transmissivity of the subsurface (i.e. the hydraulic conductivity integrated over the permeable thickness) is a major control on that drainage capacity, and so intuitively, the transmissivity should vary inversely with the degree of surface drainage dissection, as illustrated in Figure 1. Reducing the transmissivity increases partitioning of water into surface flow, which results fluvial incision closer to drainage divides (Carlston, 1963). This suggests that transmissivity controls some length scale embedded in the landscape morphology. In this paper we aim to understand the nature of this control under idealized model assumptions.

Scaling and dimensional analysis offer a powerful systematic approach for investigating models described by partial differential equations. In general, this approach allows the governing equations to be expressed in a dimensionless form, fundamental length and time scales can be identified, and dimensionless parameters controlling the scale-independent

qualitative characteristics of solutions can be obtained (Barenblatt, 1996). Studies of landscape evolution models have used such analyses to great effect, uncovering the inherent scaling properties of simple LEMs (Perron et al., 2008; Willgoose, Bras, & Rodriguez-Iturbe, 1991a; Bonetti et al., 2020; Theodoratos et al., 2018). For example Theodoratos et al. (2018) developed a dimensionless form of a simple LEM with no dimensionless parameters in the main LEM equation, suggesting that all solutions were simply rescaled versions of each other (up to differences in boundary and initial conditions). Bonetti et al. (2020) conducted a similar approach, but found that one dimensionless parameter remained in the LEM. (Note: we resolve this apparent contradiction in Section 4).

However, prior studies have not considered the role of subsurface properties or hydrology. We aim to use scaling and dimensional analysis to reveal how transmissivity controls these fundamental scales and morphologic characteristics. It will also reveal how the transmissivity interacts with other scales controlled by other parameters, such as those that determine the curvature of ridge tops that do not experience runoff.

1.4 Approach

In this study, we develop and use a new groundwater-landscape evolution model to explore how subsurface-mediated runoff generation affects long-term catchment evolution. The model solves hydraulic groundwater equations to predict the water-table location given prescribed recharge. Water in excess of the subsurface flow capacity becomes overland flow, which may detach and transport sediment, altering topographic properties that in turn affect runoff generation. Our model can support recharge rates which vary in space and time, but here we constrain the scope and consider only steady, uniform recharge. We conduct a similarity analysis that provides new insight into the dynamics behind the widely used “stream power plus diffusion” model. This analysis makes predictions which we test with a series of model simulations. Additionally, the nondimensionalization generalizes our results and reconciles contradictory dimensional analyses provided by Theodoratos et al. (2018) and Bonetti et al. (2020). We can reduce the seven dimensioned parameters of the model to four dimensionless parameters, one of which is always negligible. We present numerical results confirming the efficacy of our nondimensionalization and exploring the newly defined non-dimensional parameter space to determine how hydrologic and geomorphic parameters affect emergent hydro-geomorphic properties at geomorphic steady-state. The results show that subsurface flow capacity relative to recharge rate exerts a fundamental control on hillslope length. Additionally, an emergent relationship between three topographic metrics derived from the governing equations captures the coevolution of runoff generation and topography according to the processes considered in this study.

2 Governing equations

To investigate the effects of subsurface hydrology on landscape evolution, we couple a hydrological model to a standard model of landscape evolution. First, we derive a governing equation for topographic evolution that includes the role of space- and time-variable runoff in fluvial incision. Second, we examine the hydrological model that will generate runoff. Variable dimensions are provided in Sec. 9.

2.1 Landscape evolution

Topographic elevation $z(x, y, t)$ is assumed to evolve due to fluvial incision $E_f(x, y, t)$, hillslope diffusion $E_h(x, y, t)$, and constant baselevel change U .

$$\frac{\partial z}{\partial t} = -E_f - E_h + U \quad (1)$$

The term E_f accounts for incision into the landscape by erosion due to overland flow. The term E_h accounts for gravitational soil-transport processes that tend to smooth out landscape features. The term U accounts for the constant rate of either tectonic uplift or baselevel fall, in this case increasing topographic elevation relative to a fixed elevation boundary.

In one commonly used form of this equation, fluvial incision is described by the stream-power law, originally derived from empirical data (Howard & Kerby, 1983):

$$E_f = KA^m|\nabla z|^n \quad (2)$$

Here $A(x, y, t)$ is the upslope drainage area. In the standard streampower formulation, the exponents are $m = 1/2$ and $n = 1$. This is supported by observations of stream profile concavity that suggest $m/n \approx 0.5$, and a derivation in which incision is proportional to streampower per unit surface area, and channel width increases with the square root of discharge (Whipple & Tucker, 1999; Barnhart, Tucker, Doty, Shobe, et al., 2020). This gives the streampower incision law:

$$E_f = K\sqrt{A}|\nabla z| \quad (3)$$

This equation obscures the role of hydrological processes in the fluvial incision that drives landscape evolution. The relationship in (3) can also be derived from first principles in a way that provides a natural coupling to hydrological processes. This is accomplished by assuming the incision rate E_f is related to the excess shear stress τ from overland flow by some relationship. Frequently, this is written in the form:

$$E_f = k_e(\tau - \tau_c)^\beta \quad (4)$$

This excess shear stress formulation assumes that sediment is not redeposited within the domain (meaning that the system is assumed to be “detachment-limited”), which is widely used for upland watersheds (Howard, 1994). By explicitly treating the partitioning between subsurface and surface flow the model presented here manifests a threshold for runoff generation. While both fluvial incision and runoff generation have a dependence on slope, a steeper slope yields greater fluvial incision but less surface water flow. To focus on the spatial variation in erosion associated with hydrological processes, we will examine only the case in which there is no threshold shear stress for sediment detachment, such that $\tau_c = 0$. The shear stress generated by steady, uniform flow in a rectangular channel is:

$$\tau = \rho_w g d_f |\nabla z|, \quad (5)$$

where ρ_w is the density of water, g is the acceleration due to gravity, and d_f is the flow depth. A constitutive relation for flow resistance such as the Manning or Chezy equation can provide the flow depth d_f at a particular discharge Q . We use the Chezy equation for simplicity, which gives:

$$d_f = \left(\frac{Q}{Cw\sqrt{|\nabla z|}} \right)^{2/3} \quad (6)$$

Here we assume that the channel width w is proportional to the square root of upslope area (e.g., Snyder et al., 2003; Wohl & David, 2008):

$$w \sim \sqrt{A} \quad (7)$$

As we will show in the subsequent scaling analysis, it will be useful to express w in terms of area per contour width $a(x, y, t)$. However, the hydraulic scaling relationships for channel width are defined on the basis of catchment area A at a given cross-section (Leopold & Maddock, 1953). To make the conversion between A and a , we represent A as the product of a and a characteristic contour width v_0 , which is a chosen constant value. We will examine the physical significance of this parameter in later sections. To obtain values for w from the expression (7) we additionally require the dimensionless parameter k_w :

$$w = k_w \sqrt{v_0 a} \quad (8)$$

In this equation there is only one degree of freedom, so we are free to choose a value of v_0 for which there will always be a corresponding value of k_w to satisfy a given relationship between a and w . Ultimately, k_w will become a component of the stremppower coefficient K , while here v_0 remains separate, and has additional significance in the context of hydrological processes.

Next, we write the discharge $Q(x, y, t)$ as the product of an instantaneous runoff ratio $Q^*(x, y, t)$, upslope area A , and the average recharge rate p , $Q = pAQ^*$, and substitute into (5) and (6) to find the flow depth and shear stress.

$$d_f = \left(\frac{Q^* p \sqrt{v_0 a}}{C k_w \sqrt{|\nabla z|}} \right)^{2/3} \quad (9)$$

$$\tau = \rho_w g \left(\frac{Q^* p \sqrt{v_0 a}}{C k_w \sqrt{|\nabla z|}} \right)^{2/3} |\nabla z| \quad (10)$$

To recover the stream power formulation of the fluvial incision term, we set $\beta = 3/2$ (Tucker, 2004) in (4), representative of hydraulic detachment by plucking (Whipple et al., 2000; Tsujimoto, 1999). With these substitutions, the incision rate E_f can be written as:

$$E_f = K \sqrt{v_0} Q^* \sqrt{a} |\nabla z| \quad (11)$$

where $K = \frac{(\rho_w g)^{3/2} k_w p}{C k_w}$. This form is equivalent to (3), with time and space varying runoff accounted for in Q^* . Additionally because Q^* is dimensionless, K in (11) has units of $[1/T]$, the same as in (3).

The upslope area A is usually defined by explaining the algorithms used to calculate it in numerical schemes, which find flow directions on a discrete grid and sum the grid cell areas downslope along these flow directions. However, this approach gives the area an implicit dependence on grid cell spacing. Area per contour width a on the other hand has a precise mathematical definition that can be derived from conservation of mass (Bonetti et al., 2018, 2020). Consider the steady-state depth of water h_f across a surface where all locations contribute runoff at the same rate r . Conservation of mass for this system indicates that $\nabla \cdot (h_f u) = r$, where u is the (vector) flow velocity. Now suppose that the flow velocity at every point also has magnitude r and points in the direction of steepest descent $-\nabla z / |\nabla z|$. To satisfy continuity with this velocity, the flow depth must increase downslope. In fact, the flow depth is equal to the upslope area per contour width, $h_f = a$ (Bonetti et al., 2018). This derivation shows that, by definition:

$$-\nabla \cdot \left(a \frac{\nabla z}{|\nabla z|} \right) = 1. \quad (12)$$

We are not implying that the assumptions we have made here are necessarily characteristics of all real flow; rather these assumptions can be employed, without violating conservation of mass, to develop a condition that area per contour width must satisfy. This expression will become important in our scaling analysis in later sections, as the scaling properties of the governing equations should be independent of the numerical implementation where a grid cell width must be chosen.

Here we use a linear diffusion model of hillslope processes for E_h , which emerges by assuming that the non-fluvial sediment transport rate q_h is proportional to the local slope gradient $-\nabla z$, much as diffusion of a solute is proportional to the concentration gradient (Dietrich et al., 2003). Then by assuming $E_h \sim \nabla \cdot q_h$ from continuity, we find:

$$E_h = -D\nabla^2 z, \quad (13)$$

where D is the linear diffusion constant. While nonlinear formulations of diffusion have proven useful in explaining topography (Roering et al., 1999; Roering, 2008), here we use linear diffusion to limit model complexity. We assume that baselevel change has a constant rate U in time and space by adopting a frame of reference anchored to baselevel at the boundary of the domain. This can equivalently represent tectonic uplift or baselevel fall. This term becomes a “source” in the differential equation; without it, the topography would simply erode to a flat plane. While baselevel change is likely not steady in time in real landscapes, this assumption allows us to examine the emergent properties of steady-state solutions to the governing equation. Combining all terms together, we arrive at our governing equations for topographic evolution:

$$\frac{\partial z}{\partial t} = -K\sqrt{v_0}Q^*\sqrt{a}|\nabla z| + D\nabla^2 z + U \quad (14)$$

$$-\nabla \cdot \left(a \frac{\nabla z}{|\nabla z|} \right) = 1 \quad (15)$$

This is different from the standard streampower formulation of landscape evolution in that it includes a dimensionless runoff coefficient Q^* to account for the spatial and temporal variation in runoff across the landscape. While there is considerable uncertainty in the form of the fluvial incision term, the similarity between the form we have selected and the standard “stream power plus diffusion” formulation allows us to make use of the same nondimensionalization techniques used for the standard LEM, and has properties that will aid in implementation and analysis of results while remaining plausible within the context of the existing literature.

2.2 Hydrology

Thus far, we have made no assumptions regarding the hydrology, instead introducing a general dimensionless runoff rate $Q^* = Q/(pA)$. Any approach to representing hydrology could use the above equations by calculate appropriate values for Q^* . In our application surface water runoff is assumed to be generated by exfiltrating subsurface lateral flow (Hewlett & Hibbert, 1967) and by precipitation on saturated areas (Dunne & Black, 1970). We solve for this runoff using a quasi-3D shallow unconfined aquifer model using the Dupuit-Forcheimer approximations (e.g., Childs, 1971). The approximations are valid in locations where the vertical component is small—generally where saturated thickness is small relative to hillslope or seepage face length (Bresciani et al., 2014). While this may not be the case everywhere in our model parameter space, we are using the approximations because we cannot feasibly complete the landscape evolution simulations with the full 3D representation due to computational cost. A model of this type repre-

sents a worthwhile trade-off between accuracy and efficiency at this stage in the development of coupled groundwater-LEMs. We solve the model for lateral groundwater flow $q(x, y, t)$, and local runoff production $q_s(x, y, t)$. This model makes use of a method of regularization introduced by Marais et al. (2017) in solving for q_s that greatly improves model stability at seepage faces. Surface water discharge is calculated by instantaneously routing q_s and summing the accumulated local runoff over the area upslope of a given location. The governing equations for the hydrological model are:

$$\frac{\partial h}{\partial t} = \frac{1}{n_e} \left(p - \nabla \cdot q - q_s \right) \quad (16)$$

$$q = -h \cos \theta k_s (\nabla z_b + \nabla h) \cos \theta \quad (17)$$

$$q_s = \mathcal{G}\left(\frac{h}{b}\right) \mathcal{R}\left(i - \nabla \cdot q\right) \quad (18)$$

$$Q = \int_A q_s dA \quad (19)$$

where $h(x, y, t)$ is the aquifer thickness, n_e is the effective or drainable porosity, $\theta(x, y, t)$ is the local slope of the (presumed impermeable) aquifer base, z_b is the elevation of the aquifer base, k_s is the saturated hydraulic conductivity, and b is the permeable thickness. The regularization function $\mathcal{G}(\cdot)$ has a value of zero when the argument is less than one, and approaches 1 as the argument approaches 1. The ramp function $\mathcal{R}(\cdot)$ is zero when the argument is less than zero and takes on the argument value when it is greater than zero.

Though this model can accommodate time-variable recharge, here we consider only constant recharge at rate p . Careful examination of this model reveals that saturated areas receive “recharge” at the same rate as areas with deeper water-tables. In reality, saturated areas receive direct precipitation, while areas with deeper water-tables receive a smaller fraction as a result of losses to unsaturated zone storage and evapotranspiration from the root zone. When saturated area is a small proportion of the total area and the water-table is not too deep, this effect may be negligible. We will leave further investigation on the role of unsaturated zone dynamics to a future contribution, as this would add considerable complexity to the model.

In the cases modeled here, the permeable thickness b is treated as constant in space and time. As our model does not distinguish between mobile soil or regolith and in-place weathered or fractured rock, we will use permeable thickness as a general term for the entire permeable zone in which the shallow aquifer must be contained. Considerable uncertainty exists in the rates and mechanisms that convert fresh bedrock to permeable fractured rock and/or regolith. Many past models have used an exponential function for the production of regolith (e.g., Ahnert, 1976; Armstrong, 1976; Rosenbloom & Anderson, 1994; Tucker & Slingerland, 1997), where the production rate is a function of regolith thickness. Permeable thickness may be considered to follow a similar law, in that it tends to be thicker where the materials are more susceptible to weathering processes, where a wetter climate allows for more active subsurface weathering, and/or where erosion rates are lower. At geomorphic steady-state, both the rates of change of topographic elevation and unweathered bedrock elevation go to zero. For the latter to be the case, the production rate of weathered material must be equal to the uplift rate. When the uplift rate and regolith production coefficients are spatially uniform, permeable thickness must be also be uniform to satisfy this equilibrium. This suggests that it is reasonable to treat permeable thickness as steady and uniform across the model domain given that we are only concerned with steady-state landforms in this paper.

3 Numerical implementation

3.1 Timescale considerations

One of the primary challenges in coupling a hydrological model with a landscape evolution model is the vast difference in process timescales. While the relevant timescale for storm runoff response may be on the order of hours or even minutes, landscape evolution processes can have characteristic timescales in the tens to thousands of years. It would be too computationally expensive to run models over geologic time using appropriately small timesteps for stability and accuracy of the hydrological model. Zhang et al. (2016) identified two approaches to address this problem: online updating and offline updating. In the offline case, the hydrological model is run for many steps without updating topography, and then appropriately averaged discharge values are used to update topography over some larger geomorphic timestep. In contrast, online updating involves having a direct scaling between the hydrological timestep (e.g., one storm event) and the geomorphic timestep. Zhang et al. (2016) use an online approach, citing possible non-uniqueness of solutions in the offline approach depending on the time between geomorphic updates. Given that we consider only steady recharge in this paper, there should not be a significant difference between online and offline approaches given that the hydrological state varies gradually, only in response to changing topography. Nonetheless, our approach can be considered online updating, as we scale the geomorphic timestep as k_{sf} times the hydrological timestep: $\Delta t_g = k_{sf}\Delta t_h$. We call k_{sf} the timestep scaling factor.

3.2 Model implementation

The groundwater and landscape evolution models described above were implemented as the `DupuitLEM` Python package, which makes extensive use of existing tools from the Python-based Earth surface modeling toolkit Landlab (Hobley et al., 2017; Barnhart, Hutton, et al., 2020). Landlab includes tools for creating grids, setting boundary conditions, handling input and output, along with a diverse range of process components that modify fields on Landlab grids according to physical laws. The groundwater model described above is implemented as a component in Landlab called `GroundwaterDupuitPercolator` (D. Litwin et al., 2020).

`DupuitLEM` can handle raster, hexagonal, and irregular grids, along with zero-flux and fixed-value boundary conditions. The model base class takes components that update the hydrological state via hydrological fluxes and changes in boundary conditions, update topography via fluvial incision and hillslope diffusion, and update topography and permeable thickness via baselevel change and regolith production. Here we use the `DupuitLEM` subclass `StreampowerModel`, designed for use with the Landlab fluvial incision component `FastscapeEroder`, which solves a modified version of the Fastscape algorithm (Braun & Willett, 2013).

The hydrological state is updated with a `DupuitLEM HydrologicalModel`. All hydrological models solve for aquifer state and fluxes using the `GroundwaterDupuitPercolator` component. Surface water discharge is routed instantaneously using a D8 algorithm when the grid is a raster, or a steepest descent algorithm otherwise. In the case of steady recharge, we use the `HydrologicalModel` subclass `HydrologySteadyStreamPower`, which updates the surface water discharge by advancing the `GroundwaterDupuitPercolator`, finding surface flow directions including routing through topographic depressions, and accumulating q_s along flow directions to determine Q . With known area A and recharge rate p , we can calculate the runoff ratio $Q^* = Q/(pA)$ that appears in our streampower model, linking the hydrology to geomorphic evolution. We use a raster grid with dimensions 125x125, with three zero flux boundaries (right, left, top) and one fixed value boundary along the bottom of the model domain. The geomorphic timestep is kept constant at 45 years, while the hydrologic timestep varies as a multiple of the von Neumann stability criteria, tak-

410 ing values from approximately four hours to three days. The adaptive timestep solver
 411 of the `GroundwaterDupuitPercolator` will further subdivide the timestep to meet sta-
 412 bility criteria, while surface flow is only routed at this interval.

413 4 Scaling and similarity

414 A similarity analysis of the governing equations illuminates their fundamental con-
 415 trols and will guide the investigation conducted in the rest of this paper. Here we use
 416 an approach based on the concept of symmetry groups (Barenblatt, 1996). A symme-
 417 try group is a set of scaling transformations of variables and parameters by a constant
 418 factor that leave the governing equations unchanged due to cancellation of that factor.
 419 In essence, we seek to identify the complete set of symmetry groups and apply the trans-
 420 formations such that we consolidate or eliminate parameters that appear in the equa-
 421 tions. With this approach we arrive at a general form of the governing equations where
 422 dimensioned parameters appear in dimensionless groups. We use these emergent dimen-
 423 sionless parameters in our numerical experiments, greatly reducing the size of the pa-
 424 rameter space to explore and exposing relationships between model parameters.

425 4.1 *NoHyd* model

426 We will begin this process by considering the simplest version of the model with-
 427 out space- or time-variable runoff, such that $Q^*(x, y) = 1$ everywhere. We will call this
 428 the *NoHyd* model. The symmetry group analysis is most easily conducted when the model
 429 parameters have been rewritten as the product of characteristic scales, isolating each di-
 430 mension (time, length, etc.). Theodoratos et al. (2018) determined that there are unique
 431 characteristic scales for the vertical coordinate, the horizontal coordinate, and time h_g, ℓ_g, t_g
 432 that emerge from the “streampower plus diffusion” landscape evolution equations. Based
 433 on their analysis, we can rewrite equations (14) and (15) in terms of these scales with-
 434 out changing the units of the state variables.

$$t_g \frac{\partial z}{\partial t} = -\sqrt{\ell_g} Q^* \sqrt{a} |\nabla z| + \ell_g^2 \nabla^2 z + h_g \quad (20)$$

$$-\nabla \cdot \left(a \frac{\nabla z}{|\nabla z|} \right) = 1 \quad (21)$$

Because we have replaced three parameters, K , D , and U , in Equation (14) three characteristic scales, h_g , ℓ_g , and t_g , we can derive a system of equations for their relationships: $U = h_g/t_g$, $D = \ell_g^2/t_g$, $K\sqrt{v_0} = \sqrt{\ell_g}/t_g$. We can solve this system for the characteristic scales:

$$h_g = \left(\frac{DU^3}{v_0^2 K^4} \right)^{1/3} \quad (22)$$

$$\ell_g = \left(\frac{D^2}{v_0 K^2} \right)^{1/3} \quad (23)$$

$$t_g = \left(\frac{D}{v_0^2 K^4} \right)^{1/3}. \quad (24)$$

These definitions are slightly different from those of Theodoratos et al. (2018), as we use the area per contour width a as a state variable rather than using total drainage area A . Next we will identify the symmetry groups. We find that there are three groups, each of which allows us to scale two or more dimensioned variables by an arbitrary factor $c > 0$ and leave equations (20) and (21) unchanged.

$$\{t \rightarrow ct, t_g \rightarrow ct_g\} \quad (25)$$

$$\{z \rightarrow cz, h_g \rightarrow ch_g\} \quad (26)$$

$$\{x \rightarrow cx, y \rightarrow cy, a \rightarrow ca, l_g \rightarrow cl_g\} \quad (27)$$

The notation above can be read as, for example, “replace each occurrence of t by ct ,” and similarly for each set of symbols separated by a right-pointing arrow. For example, consider applying the first symmetry group by replacing every occurrence of t with ct . We find that when doing this, we must also replace every occurrence of t_g with ct_g in order for all c ’s to cancel. The same principle applies to the other groups as well. Note that the final group also requires that we transform the gradient operator: $\nabla^2 z \rightarrow c^{-2} \nabla^2 z$ and $|\nabla z| \rightarrow c^{-1} |\nabla z|$, which are a consequence of the transformations of x and y .

We can now choose values of c such that the characteristic scales h_g , ℓ_g , and t_g do not appear in the equations. For example, we can apply the first symmetry group, taking $c = 1/t_g$, resulting in the transformations $\{t \rightarrow t/t_g, t_g \rightarrow 1\}$. In doing so, we have effectively rescaled t into units of t_g . We will denote this dimensionless time as $t' = t/t_g$. Likewise, we can take a similar approach with application of the other symmetry groups:

$$\begin{aligned} &\{t \rightarrow t/t_g, t_g \rightarrow 1\} \\ &\{z \rightarrow z/h_g, h_g \rightarrow 1\} \\ &\{x \rightarrow x/\ell_g, y \rightarrow y/\ell_g, a \rightarrow a/\ell_g, l_g \rightarrow 1\} \end{aligned} \quad (28)$$

Applying all three transformations and defining the dimensionless state variables

$$\begin{aligned} t' &= t/t_g \\ z' &= z/h_g \\ x' &= x/\ell_g \\ y' &= y/\ell_g \\ \nabla' &= \nabla \ell_g \\ a' &= a/\ell_g \end{aligned} \quad (29)$$

we obtain the dimensionless governing equations for the landscape evolution model:

$$\frac{\partial z'}{\partial t'} = -\sqrt{a'} |\nabla' z'| + \nabla'^2 z' + 1 \quad (30)$$

$$-\nabla' \cdot \left(a' \frac{\nabla' z'}{|\nabla' z'|} \right) = 1 \quad (31)$$

No parameters appear in these rescaled equations. Intuitively, this demonstrates that all possible solutions of the *NoHyd* model can be obtained by appropriately rescaling any other solution given identical boundary and initial conditions. We would not obtain a fully parameterless model if we had chosen to write the equations in terms of area A rather than area per unit contour width a . In that case, a single parameter v_0/ℓ_g would appear in equation (31). Not accounting for this parameter effectively leaves a grid cell size dependence in the nondimensionalization, which is something we seek to avoid.

4.2 DupuitLEM model

Next we relax our constraint of uniform dimensionless runoff ($Q^* = 1$) and incorporate the hydrology equations into the scaling analysis. This model is called *DupuitLEM*.

The scaling analysis of this model extends the analysis of the *NoHyd* model, and can be found in Appendix A. To complete the analysis, we introduce two new characteristic scales: a characteristic aquifer drainage time t_d and a characteristic aquifer thickness h_a (which are also reproduced in Equations A4 and A3 respectively):

$$h_a = \frac{p\ell_g}{k_s h_g / \ell_g} \quad (32)$$

$$t_d = \frac{\ell_g n_e}{k_s h_g / \ell_g}. \quad (33)$$

The dimensionless governing equations for the *DupuitLEM* model are:

$$\frac{\partial z'}{\partial t'} = -Q^* \sqrt{a'} |\nabla' z'| + \nabla'^2 z' + 1 \quad (34)$$

$$-\nabla' \cdot \left(a' \frac{\nabla' z'}{|\nabla' z'|} \right) = 1 \quad (35)$$

$$\frac{\partial h'}{\partial t} \frac{t_d}{t_g} = 1 - \nabla' \cdot q' - q'_s \quad (36)$$

$$q' = -h' \cos^2(\arctan |\nabla' z'| h_g / \ell_g) \left(\nabla' h' \frac{h_a}{h_g} + \nabla' z' \right) \quad (37)$$

$$= -h' \frac{\nabla' h' h_a / h_g + \nabla' z'}{1 + (h_g / \ell_g)^2 |\nabla' z'|^2} \quad (38)$$

$$q'_s = \mathcal{G} \left(h' \frac{h_a}{b} \right) \mathcal{R} \left(1 - \nabla' \cdot q' \right) \quad (39)$$

$$Q^* = \frac{1}{A'} \int_{A'} q'_s dA' \quad (40)$$

where we have defined the following dimensionless variables:

$$\begin{aligned} h &= h' h_a \\ t &= t' t_d \\ q &= q' p \ell_g \\ q_s &= q'_s p. \end{aligned} \quad (41)$$

Because runoff appears as a dimensionless parameter Q^* in the geomorphic equation, we are still able to obtain a parameterless expression for topographic evolution. There are, however, four dimensionless parameter groups that we cannot eliminate. Thus, in contrast to the *NoHyd* model, all solutions of the *DupuitLEM* model do not reduce to a single solution that can be rescaled to obtain all others. We will give the dimensionless groups the following names, which will be used throughout the rest of this paper:

$$\alpha = \frac{h_g}{\ell_g} = \frac{U}{v_0^{1/3} D^{1/3} K^{2/3}} \quad \text{Characteristic gradient} \quad (42)$$

$$\gamma = \frac{b}{h_a} = \frac{b k_s h_g}{p \ell_g^2} = \frac{b k_s U}{p D} \quad \text{Drainage capacity} \quad (43)$$

$$\text{Hi} = \frac{h_g}{h_a} = \frac{k_s h_g^2}{p \ell_g^2} = \frac{k_s U^2}{p v_0^{2/3} D^{2/3} K^{4/3}} \quad \text{Hillslope number} \quad (44)$$

$$\delta = \frac{t_d}{t_g} = \frac{n_e v_0^{2/3} D^{2/3} K^{4/3}}{k_s U} \quad \text{timescale factor} \quad (45)$$

467 Here α is a characteristic gradient of the model that emerges from the geomorphic
 468 parameters. We will call γ the drainage capacity, as it is proportional to the maximum
 469 transmissivity and the characteristic topographic gradient and inversely proportional to
 470 the mean recharge rate. Hi is analogous to the Hillslope number Hi presented by Brutsaert
 471 (2005, their Eq. 10.139) and used by Harman and Sivapalan (2009), Harman and Kim
 472 (2019), and others to understand shallow groundwater dynamics. Brutsaert (2005) and
 473 Berne et al. (2005) recognize that the Dupuit-Forcheimer model can be reduced to an
 474 advection-diffusion equation on aquifer thickness, in which advection corresponds to flow
 475 driven by topographic gradients, and diffusion driven by gradients in aquifer thickness.
 476 As the factor $1/Hi = h_a/h_g$ appears as a coefficient on the diffusive term, Hi can be
 477 thought of as a Peclet number, in which large values correspond to flow primarily driven
 478 by advective forces, while small values correspond to flow primarily driven by diffusive
 479 forces (Berne et al., 2005). An analysis presented in Appendix B discusses the scaling
 480 properties of the governing equations in the special cases when Hi is small and large. Lastly,
 481 δ represents the scaling between the hydrologic and geomorphic timescales of the model.
 482 By the nature of hydrologic and geomorphic processes, we expect this ratio to be very
 483 small in all cases. Additionally, δ multiplies the time rate of change of aquifer thickness,
 484 which should also be very small here as we only consider steady recharge.

485 4.3 Predictions from scaling analysis

486 The scaling analysis will significantly improve our ability to explore and understand
 487 variability across the parameter space in the following sections. From the scaling anal-
 488 ysis alone, we can make several predictions of what we expect to see in the numerical
 489 results. In particular, we expect to find the following:

- 490 1. **Dimensionless topography from the *NoHyd* model should be identical,**
 491 **regardless of chosen h_g and ℓ_g .** If the boundary and initial conditions and the
 492 dimensionless domain size are the same, the absence of parameters in the dimen-
 493 sionless governing equations implies that the dimensionless topography should be
 494 invariant.
- 495 2. **Dimensionless topography from the *DupuitLEM* model should only be**
 496 **invariant to changes in h_g and ℓ_g when their ratio is held constant.** Be-
 497 cause the *DupuitLEM* model retains a dependence on $\alpha = h_g/\ell_g$, the invariance
 498 found for the *NoHyd* model should only occur when we keep all dimensionless pa-
 499 rameters the same, including α .
- 500 3. **Dimensionless topography should be insensitive to α when Hi is small.**
 501 In this case, relief is small relative to aquifer thickness, and we can neglect the role
 502 of topographic gradients in driving groundwater flow. We repeat the scaling anal-
 503 ysis under these circumstances (Appendix B) and find that α does not appear.
- 504 4. **Dimensionless topography should be insensitive to Hi when Hi is large.**
 505 This case is the complement to the previous in that relief is generally large rel-
 506 ative to aquifer thickness, and we can neglect the influence of gradients in aquifer
 507 thickness on groundwater flow. Again we repeat the scaling analysis under these
 508 circumstances (Appendix B) and find that Hi does not appear.

509 5 Results

510 We explore the properties of the scaled model through a series of simulations de-
 511 signed to sample the nondimensional parameter space of α , γ , and Hi . While the timescale
 512 parameter δ does vary as we vary hydrological parameters, this effect should be negli-
 513 gible for reasons previously stated. First, we test the predictions made from the scaling
 514 analysis through a series of simulations involving both the *NoHyd* model and the *DupuitLEM*
 515 model. Second, we use the *DupuitLEM* model to explore topographic and runoff vari-
 516 ation with varying drainage capacity γ and hillslope number Hi .

We evaluated the condition of steady-state topography on the basis of change in mean dimensionless relief R_h/h_g , where R_h is the mean value of elevation z . For runs of the *NoHyd* model and runs of the *DupuitLEM* model where $\gamma < 1$, the results show clear indications of steady-state, as the absolute value of dimensionless rate of relief change $|\frac{dR_h/h_g}{dt/t_g}|$ declines below 10^{-10} . In cases with larger γ , perturbations continue through time in the absolute value of relief change. We run the model at least until there is no decreasing trend in the absolute value of relief change. Times to meet these conditions range from approximately 300–2000 t_g (around 7–45 million years given the dimensional input parameters).

5.1 Confirmation of scaling and similarity

The numerical results confirm the predictions of our scaling analysis. Rows of Figure 2 labelled with capital letters correspond to the first three predictions in Subsection 4.3, while Figure 3 corresponds with the fourth prediction from Subsection 4.3.

Addressing the first scaling prediction, in Figure 2A (i, ii, iii) we show that ℓ_g can be varied independently from h_g (changing α) with the *NoHyd* model and we can still obtain visually and numerically identical results in the rescaled coordinate system (x', y', z') . The same similarity appears when h_g is varied independently while ℓ_g remains constant (i, iv, vi) and when h_g and ℓ_g are varied together (i, v, vii). The mean absolute difference in z' between all model runs is less than $10^{-13}\%$ of total relief. These results confirm the scaling found by Theodoratos et al. (2018), showing that the vertical and horizontal dimensions possess distinct and independent scaling relationships.

Next we address the second scaling prediction that the vertical and horizontal length scales should not scale independently in the *DupuitLEM* model, unless $Hi \ll 1$. Figure 2B shows the same scaling of h_g and ℓ_g implemented in Figure 2A, now using the *DupuitLEM* model with a large hillslope number $Hi = 5$ and moderate drainage capacity $\gamma = 2.5$. As ℓ_g is increased independent of h_g (i, ii, iii), α decreases and the distance between channels appears to increase. Similarly as we increase h_g while holding ℓ_g constant (i, iv, vi), α increases and we observe a decrease in spacing between channels. These appear at first to be counterintuitive results: when relief is smaller (larger), we might expect weaker (stronger) topographic gradients driving groundwater flow, and therefore more (less) surface runoff. However because we hold drainage capacity constant, we account for this effect. This is most clearly seen when we rewrite $\gamma = \frac{bk_s h_g / \ell_g}{p\ell_g}$, where the factor h_g/ℓ_g appears in the numerator. In other words, other terms in γ must be changed in order to keep the whole dimensionless group constant. On the other hand, consider where α appears in the dimensionless governing equations (38) or alternatively (39). These show that the dimensionless groundwater specific-discharge in fact has an inverse dependence on α^2 : increasing (decreasing) α will lead to smaller (larger) dimensionless groundwater specific-discharge, and therefore more (less) surface runoff. More intuitively, consider that the gradients driving flow and cross-sectional area through which flow moves downslope are both relative to the aquifer base. Thus, increasing the slope and holding all other factors constant results in smaller gradients relative to the base, and smaller cross-sectional area through which the flow must move.

It is only when h_g and ℓ_g are varied together (i, v, vii), keeping α constant, that topography remains invariant in the rescaled coordinates. The greatest difference in mean relief between runs is 0.20%. While sufficient to confirm the scaling analysis, this difference is larger to that observed in 2A due to isolated areas that develop slightly different drainage patterns. This is likely as a result of small numerical differences between the groundwater model solutions early in the evolution of topography.

Third, we address the scaling prediction that when the hillslope number Hi is small, vertical and horizontal dimensions should scale independently, and thus the dimensionless results should be independent of the characteristic gradient α . When Hi is small,

relief is small relative to the characteristic aquifer thickness, and as a result relief should not play a strong role in generating hydraulic gradients that drive flow. In these simulations where permeable thickness is particularly deep relative to the domain size, we caution that the Dupuit-Forchheimer solution may be significantly different from an equivalent 3-dimensional flow solution. Figure 2C shows the results of the same variation in h_g and ℓ_g as Figure 2B, but now with $Hi = 0.01$. Here we find less dependency of the results on α than when $Hi = 5.0$, particularly when $\alpha < 0.05$. Plots (i, iv, vi) show reduced dependency on α , with a maximum 51% difference in mean relief, in comparison to 145% difference when $Hi = 5.0$. There is less variation in plots (i, ii, iii), with 3.9% difference in mean relief, in comparison to 87% difference in mean relief when $Hi = 5.0$. This partially confirms what we expect from the scaling analysis, but suggests some additional dependency on α or h_g .

Last, we address the scaling prediction that when the hillslope number Hi is large, the topography should not be sensitive to Hi . In this case, hydraulic gradients are primarily driven by topographic gradients, and Hi no longer appears in the dimensionless governing equations. Figure 3 shows results with increasing Hi , with $\alpha = 0.15$ and $\gamma = 2.5$ in all cases. Topography is visually and numerically similar. The difference in mean relief between cases when $Hi = 20.0$ and $Hi = 40.0$ is 0.7%. These results demonstrate the efficacy of our scaling analysis. However in the results going forward, we will generally work with values of Hi in between the those tested in the special cases here, and thus we will not be able to neglect α or Hi .

5.2 Sensitivity to dimensionless hydrologic parameters

Varying the drainage capacity γ and hillslope number Hi in the numerical simulations suggest that landscape and climate properties affecting shallow groundwater flow have major effects on topography. There are strong differences in topography between model runs when dimensionless parameters describing these factors are varied. In particular, the evolved topography depends strongly on γ , where low γ correlates with low transmissivity, and a characteristic aquifer thickness that is large relative to permeable thickness. When $\gamma = 0.5$, the lowest value shown in Figure 4, the results look very similar to those obtained with the *NoHyd* model. In these cases the entire landscape experiences some overland flow and erosion, which is apparent in the spatial distribution of runoff Q^* shown in Figure 6. In contrast, high γ cases produce broad interfluves on which $Q^* = 0$, as the water-table sits further below the surface. As a result these areas do not experience surface erosion. To a lesser degree, the hillslope number affects the steady-state topography as well, where increasing hillslope number increases the degree to which topographic gradients, rather than gradients in aquifer thickness, drive groundwater flow. Here we increase Hi by increasing the hydraulic conductivity, while decreasing permeable thickness b in order to hold the drainage capacity γ constant. The cross-section plots in Figure 5 confirm that permeable thickness is larger when Hi is small. The topographic effect of this difference in permeable thickness appears to be greatest when drainage capacity is large, suggesting that there is an interaction between the two parameters. In large drainage capacity cases, increasing Hi generally decreases the spacing between channels.

Distributions of Q^* represent the spatial variability in runoff that emerges from our coupled geomorphic-hydrologic model under conditions of steady, uniform recharge. These distributions confirm that the extent of areas contributing runoff tends to decrease with increasing drainage capacity, and to a lesser extent with decreasing hillslope number. Figure 6B shows cumulative distribution functions of Q^* for each model run, indicating the proportion of the landscape where Q^* is less than a particular value on the x-axis. Strikingly, we see that areas that contribute no runoff ($Q^* = 0$) first appear exactly when $\gamma = 1$ (third row from the bottom). This holds for smaller and larger values of α as well (see Figures S3, S6). It is at this point that the spatial variability in Q^* is maximized:

620 at lower values all areas contribute some runoff, while above this value, most areas contribute no runoff at all. As γ is the ratio of the characteristic aquifer thickness h_a to the
 621 permeable thickness b , a value of 1 should indicate that a “characteristic hillslope” has
 622 just become saturated, which appears to be in agreement with our results. This is a pow-
 623 erful demonstration of the effectiveness of this nondimensionalization.

625 In Figure 6C, the proportion of numerical grid nodes with a dimensionless runoff
 626 rate $Q^* > 0.5$ indicates extensive saturation in low γ cases with minor sensitivity Hi
 627 values; the extent of runoff contributing areas declines slightly more rapidly when Hi is
 628 large. For comparison, we also plot the proportion of the landscape with positive cur-
 629 vature, which shows a more gradual change with γ .

630 The previous section evaluating the scaling properties of the model results showed
 631 that the characteristic gradient α has a significant effect on topography in most cases
 632 where Hi is not very small. The supplemental material includes figures showing the re-
 633 sults of varying γ and Hi with higher and lower values of α than those shown here. While
 634 the results for large drainage capacity do show some differences, the fundamental pat-
 635 terns seen, including transitions in morphology and runoff generation at $\gamma = 1$, remain
 636 the same.

637 Clearly subsurface hydrology is having a strong effect on topography in this model.
 638 With increasing ability to drain water through the subsurface (large γ), less surface drainage
 639 is needed, and consequently, the spacing between streams is greater. When drainage ca-
 640 pacity is larger, the landscape is generally steeper, and saturated areas and erosion are
 641 restricted to narrow incised regions. In contrast, landscapes with lower drainage capac-
 642 ity (smaller γ) have larger source areas of overland flow extending across more of the land-
 643 scape, and consequently more areas of active water erosion across the landscape. The
 644 patterns of Q^* indicate that $\gamma = 1$ defines the transition between landscapes that evolve
 645 with these two behaviors.

646 6 Emergent properties at landscape equilibrium

647 6.1 Topographic analysis: steepness and curvature

648 The landscapes shown in Figures 2, 4 and 6 reveal the visually striking influence
 649 of hydrological properties on landscape form. However, there is still much more we can
 650 learn about the controls on these emergent properties, guided by the form of the gov-
 651 erning equations. Furthermore, we would like to be able to develop some quantitative
 652 understanding that relates readily observable topographic features to hydrological prop-
 653 erties that are more difficult to measure. The relationships between model parameters
 654 and emergent hydrologic and geomorphic properties will be the focus of this section.

655 Commonly, properties of stream channels and entire landscapes are examined by
 656 plotting local slope versus accumulated area (e.g., Tarboton et al., 1989; Willgoose, Bras,
 657 & Rodriguez-Iturbe, 1991b; Dietrich et al., 1993). Results form point clouds where zones
 658 of distinct behavior can be identified (Perron et al., 2008). Recently, Theodoratos et al.
 659 (2018) showed that the topography resulting from the streampower-linear diffusion LEM
 660 may be analyzed by examining relationships between what they term the incision height
 661 $\sqrt{A}|\nabla z|$ and Laplacian curvature $\nabla^2 z$. (Theodoratos & Kirchner, 2020b) refer to $\sqrt{A}|\nabla z|$
 662 as steepness, so here we will adopt similar terminology, with one difference: to match
 663 the form of our governing equations, we define steepness as $\sqrt{a}|\nabla z|$, using area per con-
 664 tour width a rather than area A . Steepness and curvature emerge naturally from the steady-
 665 state form of the governing equation for topographic evolution (20). Setting the time rate
 666 of change equal to zero, and rearranging, we obtain the following relationship:

$$\nabla^2 z = \ell_g^{-3/2} Q^* \sqrt{a} |\nabla z| - \frac{h_g}{\ell_g^2} \quad (46)$$

which has the equivalent dimensionless form:

$$\nabla'^2 z' = Q^* \sqrt{a'} |\nabla' z'| - 1 \quad (47)$$

When runoff generation is spatially uniform and therefore $Q^* = 1$ for all (x, y) , as in the *NoHyd* model, there is a linear relationship between steepness and curvature, with a slope of unity and intercept of -1 in dimensionless coordinates, as observed by Theodoratos et al. (2018). While this definition of steepness is contingent on the particular exponents on area and slope, Theodoratos et al. (2018) showed that this relationship can be generalized to any exponent values, albeit with significantly more complicated formulas.

Figure 7 shows topography from a run of the *NoHyd* model in slope-area and steepness-curvature space. The results show the expected slope and intercept in the steepness-curvature plot. All of the variability that appears in the slope-area space collapses onto a single line in steepness-curvature space, making steepness-curvature plots powerful tools for examining model behavior. Observing this relationship in the numerical solution also demonstrates that the model accurately reproduces the analytical result at steady-state.

Furthermore, deviations created by the introduction of hydrologic variability with Q^* should be readily apparent when plotting steepness versus curvature. When we use the *DupuitLEM* model, plotting $Q^* \sqrt{a'} |\nabla' z'|$ rather than $\sqrt{a'} |\nabla' z'|$ versus curvature would again result in a linear relationship. Through topographic analysis alone, however, steepness and curvature are available while Q^* is not. Quantifying the relationship between these topographically-derived quantities and Q^* across each steady-state landscape in our nondimensional parameter space thus supports quantifying hydrological function based upon topography.

Slope-area and steepness-curvature plots for selected model runs with different values of drainage capacity γ and hillslope number H_i are shown in Figure 8. The steepness-curvature relationships when drainage capacity is small show close agreement with the theoretical relationships derived from the *NoHyd* model (dotted black line). This is consistent with the observed values of Q^* , which are close to unity at most nodes. With increasing drainage capacity, there is an apparent separation between points that conform to the theoretical relationship and points that maintain constant negative curvature $\nabla^2 z = -h_g/\ell_g^2$. The difference between these behaviors is revealed in the values of Q^* . Areas in yellow have $Q^* \approx 0$, and form the zone of constant negative curvature. This is exactly what we would expect from the solution to the steady-state equation (47) in the absence of the fluvial incision term. Points in this zone are divergent hillslopes that do not reach surface saturation. Areas in blue have $Q^* \approx 1$, essentially conforming to the same relationship observed for the *NoHyd* model. Points in this zone are the fluvial valleys that are fully saturated and have discharge approximately equal to upslope area times the recharge rate. This indicates that at these locations the vast majority of water is moving over the surface rather than through the subsurface. A limited number of points fall in between these two end members of behavior. These are the channel heads and other areas of limited runoff contribution, where $0 < Q^* < 1$. When $\gamma > 1$, the proportion of points in this intermediate space appears to decrease with increasing γ .

Slope-area plots do show separation between these behaviors, though the end members of behavior are not nearly as distinct. Differences between channel and hillslope morphology are also apparent in map view plots of steepness and curvature (Figure 9). While steepness does seem to provide an indication of increasing channelization in the low drainage capacity cases, in the high drainage capacity cases, it takes on unusual swirling patterns

on hillslopes, in part due to the D8 flow routing method. These are of little consequence in the context of processes acting in the model, because on these hillslopes $Q^* \rightarrow 0$ and therefore the fluvial incision term there also goes to zero. Map view curvature plots show that in low drainage capacity cases, areas of negative curvature are restricted to narrow areas near the ridges, while extensive areas have near zero or positive curvatures, indicating predominantly concave-upward terrain. In comparison, in high drainage capacity cases, most points obtain a constant negative curvature, representing convex-upward hillslopes, while the channels obtain large positive curvatures as a consequence of the steep adjacent hillslopes.

6.2 Hydromorphic balance

How can we understand the separation between channel and hillslope behavior that appears in the *DupuitLEM* model results? While there is a unique relationship between steepness and curvature for the *NoHyd* model, this is no longer the case for the *DupuitLEM* model, indicating that some information is not captured by these terms alone. The missing piece, as equation (47) shows, is Q^* . That is, there is a unique relationship between steepness, curvature, and Q^* . If we would like to know Q^* , one approach would be to solve for Q^* and explore how it could be determined from the governing equations. Using the equation for topography at steady-state (20), we find Q^* as a function of the parameters, steepness, and curvature.

$$Q^* = \ell_g^{3/2} \frac{\nabla^2 z}{\sqrt{a} |\nabla z|} + \frac{h_g}{\sqrt{\ell_g}} \frac{1}{\sqrt{a} |\nabla z|} \quad (48)$$

We will call this equation the *Geomorphic Balance*. Results of plotting Q^* versus the right hand side of this equation are shown in Figure 11A. Like the relationship between steepness and curvature for the *NoHyd* model, the geomorphic balance shows a tight linear relationship. In other words, most places in the landscape have topography that is closely coupled with the runoff at that location, as predicted by the governing equations. Deviation from the 1:1 line in Figure 11A is an indication that the hydrologic state and geomorphic state are not completely in equilibrium with one another. These deviations likely have a similar origin to the perturbations in relief as the model evolves toward topographic steady-state that we noted previously. Both indicate that subtle adjustments between the hydrologic and geomorphic states persist in the evolution of the modeled landscapes. This demonstration of dynamic equilibrium has similarities to natural settings where adjustment to small perturbations is persistent even in landscapes that are considered to be near geomorphic steady-state.

Unfortunately in most cases where one might want to apply the *Geomorphic Balance* to real data to determine spatial patterns of runoff and saturation, the geomorphic length scales h_g and ℓ_g are unknown. While the *NoHyd* model has distinct relationships between landscape properties and h_g and ℓ_g , explored by Theodoratos et al. (2018), those relationships break down with the addition of subsurface hydrology. Even if we were to estimate h_g and ℓ_g through geomorphic methods, the uncertainty in direct estimates these parameters is likely far too great to constrain Q^* in (48).

The governing hydrologic equations offer a complementary solution for Q^* . At hydrological steady-state, for steady recharge at rate p , the expression for conservation of mass (16) can be written as:

$$p = \nabla \cdot q + q_s \quad (49)$$

This should be a reasonable representation of our results, as the recharge rate is constant, and other properties vary slowly with time. Integrating this water balance over the watershed area, A , and using Leibniz' rule to evaluate the integral of the divergence term:

$$\int_A pdA = \int_A (\nabla \cdot q + q_s) dA \quad (50)$$

$$pA = \iint \nabla \cdot q dx dy + Q^* pA \quad (51)$$

$$pA = \oint_S q \cdot \hat{n} dS + Q^* pA \quad (52)$$

where S is the catchment boundary and \hat{n} is the unit normal vector on the catchment boundary. If we assume that the catchment boundary is a no-flux boundary except for the outlet with characteristic contour width v_0 , then this reduces to:

$$pA = qv_0 + Q^* pA \quad (53)$$

This also assumes that groundwater flux is directed out of the watershed, which is a tenuous assumption for deeper regional aquifers but perhaps is appropriate for the shallow near-surface aquifers that tend to produce return flow and near-channel areas of surface saturation during rainfall events. We selected the characteristic contour width v_0 here to be the same as the contour width used in (8), so the relationship $A = v_0 a$ still holds. Next we substitute the expression for groundwater flow (17). Assuming gradients are directed out of the watershed, we can take the absolute value of gradients for similarity to the geomorphic balance.

$$pA = v_0 k_s h (|\nabla h| + |\nabla z|) \cos^2(\theta) + Q^* pA \quad (54)$$

then substituting $A = av_0$ and rearranging to solve for Q^* :

$$Q^* = 1 - \frac{k_s h}{p} \frac{(|\nabla h| + |\nabla z|) \cos^2(\theta)}{a} \quad (55)$$

By limiting ourselves to locations where the water-table has reached the land surface so that the aquifer base and land surface are parallel, we can set $h \rightarrow b$ and $\nabla h \rightarrow 0$.

$$Q^* = 1 - \frac{k_s b}{p} \frac{|\nabla z| \cos^2(\theta)}{a} \quad (56)$$

This is our *Hydrologic Balance* expression for Q^* . Contained in this expression is a modified version of the topographic index $\frac{a}{\nabla z \cos^2(\theta)}$, where we have retained the cosine term for similarity to the governing equation for groundwater flow. It is appropriate that topographic index should appear in this equation, as it has been shown to be a useful tool for understanding geomorphically-driven hydrological behavior (Beven & Kirkby, 1979). The results of plotting Q^* against the right hand side of (56) are shown in Figure 11B. Correlations are not as strong as geomorphic balance.

Investigation revealed that differences between modeled results and our analytical solution result from differences in the style of surface versus subsurface flow routing. Subsurface flow is calculated in a “diffusive” sense by measuring fluxes in or out on all links connecting nodes of the computational mesh. In contrast, surface routing is cal-

culated with an “advective”, steepest-descent approach, where all flow is routed downslope from one single node to another. The analytical solution assumes that the recharge on the upslope area, which we calculate with the “advective” method, is the total flow that is partitioned between surface and subsurface flow at a node. If all flow were routed with the “advective” method, we would expect the modified topographic index to have a 1:1 correspondence with Q^* . However, Figure 10 shows that there is not a unique relationship between the two, particularly for small and intermediate values of topographic index. However, curvature (colors), which better captures the degree of landscape convergence or divergence driving groundwater flow, is able to explain the trend in Q^* at a given value of topographic index. While this pattern appears here as a consequence of our model choice, it may capture something intrinsic about reality in which surface flow is rapid and generally channelized in a single direction, while groundwater flow is more gradual and diffusive in nature. With two expressions for Q^* , one hydrologic in (56) and one geomorphic in (48), we can combine these expressions by eliminating Q^* and obtain:

$$1 - \frac{bk_s}{p} \frac{|\nabla z| \cos^2(\theta)}{a} = \ell_g^{3/2} \frac{\nabla^2 z}{\sqrt{a} |\nabla z|} + \frac{h_g}{\sqrt{\ell_g}} \frac{1}{\sqrt{a} |\nabla z|} \quad (57)$$

or equivalently:

$$0 = \frac{bk_s}{p} \left(\frac{|\nabla z| \cos^2(\theta)}{a} \right) + \ell_g^{3/2} \left(\frac{\nabla^2 z}{\sqrt{a} |\nabla z|} \right) + \frac{h_g}{\sqrt{\ell_g}} \left(\frac{1}{\sqrt{a} |\nabla z|} \right) - 1 \quad (58)$$

We call this expression the *Hydromorphic Balance*. It describes a fundamental relationship between steepness, curvature, and topographic index that emerges from the governing equations. Using the same nondimensionalization as previously, (58) can be rewritten as:

$$0 = \gamma \frac{a'}{\nabla' z' \cos^2(\theta)} + \frac{\nabla'^2 z'}{\sqrt{a'} |\nabla' z'|} + \frac{1}{\sqrt{a'} |\nabla' z'|} - 1 \quad (59)$$

This relationship is the expanded equivalent of the linear relationship between steepness and curvature shown in the *NoHyd* model case, where an additional dimension, the modified topographic index, is needed to capture the effects of runoff generation from saturation excess overland flow. Figure 12 shows the hydromorphic balance relationship (transparent gray surface) and modeled topography (points colored by Q^*) for three cases: the *NoHyd* model case (A), a low drainage capacity case (B), and a high drainage capacity case (C). Recall that the *NoHyd* model case effectively has a drainage capacity of zero, as all precipitation becomes surface runoff. We plot the log of the modified topographic index to improve readability of the figure and to be consistent with the conventional definition of topographic index (Beven & Kirkby, 1979). In the *NoHyd* case, all points fall on a plane that collapses to a line in steepness and curvature space. At higher subsurface capacity, places with lower topographic index (places less likely to contribute runoff) have lower curvature, as predicted by the *Hydromorphic Balance*. Locations where there is no surface runoff ($Q^* = 0$) do not fall on the surface, as the *Hydromorphic Balance* was only derived for locations where $Q^* > 0$.

While there may be limitations to the application of the *Hydromorphic Balance* for quantitative terrain analysis (for example, estimating the transmissivity bk_s , which appears as a coefficient in Equation (58)), it nonetheless has explanatory power for topography observed in our numerical simulations. Careful application to real datasets could provide evidence supporting the importance of subsurface flow processes for runoff generation and landscape evolution.

821 6.3 Emergent hillslope length

822 It is visually apparent in our results that emergent length scales of the ridge-valley
 823 topography increase with drainage capacity. This can be quantified by measuring and
 824 comparing the average hillslope length L_h across the parameter space. Here, we define
 825 L_h as the mean distance from hillslope points to the nearest channel. This is inversely
 826 proportional to twice the drainage density, where drainage density is calculated with the
 827 method described by Tucker et al. (2001). Hillslope length is of particular interest in the
 828 context of hydraulic groundwater theory, where it is both an important control on hill-
 829 slope storage and characteristic response time (Harman & Sivapalan, 2009; Troch et al.,
 830 2003). A measure of hillslope length depends on the delineation of channel locations. While
 831 it is common to use threshold values of steepness index to identify channels (e.g., Tucker
 832 et al., 2001), this implicitly assumes a relationship between steepness and incision, which
 833 is not the case in the *DupuitLEM* model. Instead, we identify channels as points of positive
 834 Laplacian curvature ($\nabla^2 z > 0$), where fluvial incision is the dominant geomorphic
 835 process.

836 We can use the hydromorphic balance to predict the scaling relationship between
 837 hillslope length and the drainage capacity γ . We begin with the hydrologic and geomor-
 838 phic balance expressions, equations (56) and (48). This time, rather than combining to
 839 eliminate Q^* as we did previously, we can combine to eliminate the topographic gradi-
 840 ent $|\nabla z|$. Since we have defined channels as places where $\nabla^2 z > 0$, channel heads can
 841 be defined as places where $\nabla^2 z = 0$. We can apply the latter condition to the geomor-
 842 phic balance to obtain an expression for the critical upslope area per contour width a_c
 843 at channel heads. We cannot eliminate all instances of the gradient in the hydromorphic
 844 balance, as it is present in the term $\cos(\theta) = \cos(\arctan |\nabla' z' h_g / \ell_g|)$. Here we will make
 845 the assumption that the dimensionless gradient in this term is equal to one at channel
 846 heads, such that $\cos(\theta) \approx \cos(\arctan(\alpha))$. Assuming θ is similar at channel heads across
 847 our parameter space, this assumption should only affect the coefficient scaling γ and hill-
 848 slope length. We must also choose a value for Q^* in order to find a solution for both the
 849 *Hydrologic balance* and *Geomorphic Balance*, as we have not eliminated it in this case.
 850 Our results show that Q^* can vary substantially at locations of zero Laplacian curva-
 851 ture (not shown), but here we will introduce a constant characteristic value Q_c^* for the
 852 purposes of finding a solution. Applying these conditions, we find that the hydromor-
 853 phic balance gives an expression for the area per contour width at channel heads a_c :

$$\frac{a_c}{l_g} = \left(\frac{\gamma/Q_c^{*2}}{1 + \alpha^2} \right)^{2/3} \quad (60)$$

$$= \left(\frac{bk_s}{pQ_c^{*2}} \frac{h_g}{h_g^2 + l_g^2} \right)^{2/3} \quad (61)$$

854 or, expanding out the definitions of h_g and l_g , we can solve for the critical area at
 855 channel heads, $A_c = a_c v_0$:

$$A_c = \left(\frac{v_0 b k_s}{p Q_c^{*2}} \hat{h}_g \right)^{2/3} \quad (62)$$

856 where \hat{h}_g is the inverse sum of two vertical length scales defined by the geomorphic
 857 variables:

$$\frac{1}{\hat{h}_g} = \frac{K}{U} + \frac{U}{\sqrt[3]{D^2 K v_0^2}} \quad (63)$$

The scaling confirms our previous observations that increasing the drainage capacity γ leads to greater spacing between channels, and therefore larger source areas at channel heads. Intuitively, this suggests that the landscape is less dissected when more flow drains through the subsurface. The expanded relationship shows a similar story: increasing $v_0 b k_s$ leads to larger contributing areas at channel heads, while increasing recharge rate p or effectiveness of fluvial incision relative to uplift lead to smaller contributing areas at channel heads. From here we further assume that the hillslope length at channel heads is proportional to the area per contour width, and thus $L_h/\ell_g \sim \gamma^{2/3}$. Despite the crudeness of this estimate, Figure 13 shows that this scaling is in agreement with the model results when $\gamma > 1$. Supplemental Figure S7 shows that hillslope length does scale linearly with critical area per contour width. Additionally, Figure S8 shows an equivalent to Figure 13 which confirms the scaling with γ using an alternative metric that is very close to the definition of a_c used in the analysis here.

7 Discussion

7.1 Hydrogeomorphic coevolution

The results presented here constitute one possible way that landscape history can be used to understand current hydrological processes by quantifying the coevolution of hydrological processes with landscape form (Harman & Troch, 2014; Troch et al., 2015). Prior attempts to use coevolution to understand hydrological flow paths and processes focus on evolving subsurface properties. Jefferson et al. (2010) and Yoshida and Troch (2016) explore how flow paths evolve on constructional basaltic terrains, where porous young terrains tend to be highly permeable and drain flow vertically, while chemical weathering of basalt tends to progressively block flow paths with clays, leading to increased prevalence of lateral flow on older terrains. Both studies use space-for-time substitution to explore temporal changes in drainage density, but find contradictory trends, suggesting that underlying processes of drainage and erosion are still not well enough understood in these landscapes. In contrast, recent work in denudational landscapes has focused on coevolution of subsurface flow paths and subsurface structure through the propagation of weathering fronts, in which porosity and permeability tend to increase as reactions take place and weathering products are removed (Harman & Kim, 2019; Harman & Cosans, 2019; Brantley, Lebedeva, et al., 2017). In these studies, continuous incision of streams is often used as a boundary condition to which hillslopes respond. In this study, we took a complementary approach, enforcing constant permeable thickness, hydraulic conductivity, and porosity, while exploring surface geomorphic evolution. We found that subsurface flow plays a critical role in setting hillslope length, which may in turn affect the hydraulic gradients and flow rates that affect subsurface weathering processes. Approaches focused on surface and subsurface may be unified to formulate more general theories of the evolution of denudational landscapes that could provide new insights or constraints on critical zone evolution hypotheses (Riebe et al., 2017).

7.2 Drainage density, lithology and transmissivity

One of the predictions of our model is a scaling relationship between subsurface drainage capacity and channel head contributing area per contour width, which should be comparable to a scaling relationship between transmissivity and hillslope length or drainage density. Linking drainage density to hydrological processes has long proven difficult. Early work on this topic by Carlston (1963) suggested an inverse relationship be-

903 between drainage density and transmissivity, in agreement with what we observe in our nu-
 904 matical and analytical results. Carlston (1963) presented a negative correlation between
 905 drainage density and average baseflow for 13 humid climate watersheds as evidence of
 906 this relationship, though Dingman (1978) correctly argued that there is little physical
 907 basis to assume that mean baseflow scales with transmissivity. Challenges in estimat-
 908 ing landscape scale transmissivity were clearly the limiting factor in this study, and they
 909 remain such today.

910 In other cases, factors not related to permeability may affect observed relationships.
 911 As mentioned previously, Jefferson et al. (2010) and Yoshida and Troch (2016) exam-
 912 ined relationships between drainage density and age in basaltic landscapes, where per-
 913 meability is expected to decrease and drainage density to increase with time. They found
 914 contradictory trends in drainage density with age, despite the fact that both studies found
 915 that older, less permeable watersheds had the expected flashier, less subsurface-dominated
 916 runoff response. Other non-hydrological factors may be playing a larger role in control-
 917 ling drainage density in certain sites. Recent studies using large sample sizes and high-
 918 resolution topography have examined relationships between drainage density and broad
 919 ranges of environmental controls, and have again come to disagreement. Sangireddy et
 920 al. (2016) concluded that lithology has no significant effect on drainage density among
 921 the 101 sites they examined. Meanwhile, Luo et al. (2016) examined drainage density
 922 across the contiguous United States and concluded that lithology is the dominant con-
 923 trol in most regions other than coastal plains. While Luo et al. (2016) also examined hy-
 924 draulic conductivity as a potential control on drainage density, finding it to be the dom-
 925 inant control in one small area in the interior of the United States, the dataset used was
 926 itself derived from lithology and grain size data (Gleeson et al., 2014). Largely unknown
 927 covariation of many geomorphic and hydrologic properties with lithology is likely a source
 928 of uncertainty in the opposing trends observed in the previously mentioned studies. Con-
 929 sider, for example, how hydraulic conductivity of soils on a certain lithology covaries with
 930 hillslope transport rates, or bedrock erodibility. Untangling these covariations would be
 931 a useful research direction for continued understanding of landscape-hydrology coevo-
 932 lution.

933 Here we have examined the influence of subsurface hydrological conditions relative
 934 to climate (through γ and H_i) on topography in detail. The significance of this model
 935 is not that it accurately predicts the dynamics in a particular place, but that it captures
 936 the essence of a particular interaction between topography and subsurface properties via
 937 subsurface-driven runoff generation. With better datasets to help us understand the varia-
 938 tion of subsurface properties in space, and covariation of hydrologic and geomorphic
 939 properties with lithology, we may use the information generated here to understand how
 940 the effects we have exposed here are manifested in real landscapes.

941 7.3 Scaling and typology of landscapes

942 Our similarity approach expands upon the analysis of Theodoratos et al. (2018)
 943 and Bonetti et al. (2020). The analysis conducted by Theodoratos et al. (2018) showed
 944 that by selecting appropriate length and time scales, a standard form of the streampower-
 945 linear diffusion LEM—which uses A rather than a and does not consider an incision thresh-
 946 old or runoff coefficient—was parameterless, and thus had only a single landscape typology—
 947 assessed on the basis of topography—that could be rescaled to obtain every result the
 948 model could produce. As pointed out by Bonetti et al. (2020), the streampower-linear
 949 diffusion LEM does have an additional parameter, which is unaccounted for in Theodoratos
 950 et al. (2018) because the authors do not expose the differential equation that defines the
 951 upslope area per contour width. With this equation expressed, Bonetti et al. (2020) de-
 952 velop a nondimensionalization where one parameter remains, similar to the Peclet num-
 953 ber that appears in Perron et al. (2008). Our analysis of the streampower-linear diffu-
 954 sion LEM (called the *NoHyd* model here) shows that a parameterless set of equations

can still be obtained from the governing equations when accounting for the upslope area differential equation. We show that, contrary to Bonetti et al. (2020), there is a single typology for the *NoHyd* model, which can be rescaled to obtain all results the model may produce.

We develop the scaling analysis further by including the effects of runoff generated from shallow unconfined groundwater flow. This introduces four dimensionless parameters, of which three are important for the emergent topography. With this model, there is no longer a single landscape typology, but variation in form dependent on how flow is partitioned between surface and subsurface γ , the degree to which topography drives groundwater flow H_i , and the landscape gradient generated by underlying geomorphic processes α .

Other typologies are certainly possible to obtain through the addition of other geomorphic or hydrologic processes, including a fluvial incision threshold (Theodoratos & Kirchner, 2020a). While at first it may appear that our runoff generation factor Q^* should have a similar effect—and consequently produce a similar typology—to a fluvial incision threshold, this is not the case, as their dependence on topographic slope is opposite. A given threshold for surface-water erosion is more likely to be exceeded when topographic gradient is steeper, because the flow will tend to exert a higher tractive stress on the surface. However, surface water flow should be less likely to occur on steeper slopes, as hydraulic gradients in shallow aquifers will increase, increasing subsurface flow capacity. Consequently, fluvial incision threshold and runoff generation thresholds should produce different characteristic typologies in topography. The model we present here is unique in that it expresses feedbacks between hydrologic and geomorphic processes, which consequently link landscape typology to hydrologic function. While we have limited our consideration in this study to only the most basic of geomorphic processes, the scaling framework presented here could be readily expanded to include other processes should they be necessary to capture a particular environment or hydrogeomorphic feedback.

7.4 Characteristic contour width and valley transmissivity

We first introduced the concept of a characteristic contour width v_0 in order to write the channel scaling relationship (Equation 7) in terms of upslope area per contour width a rather than upslope area A . This proved useful in subsequent scaling analyses, where we developed a new parameterless scaling of the governing geomorphic equations that is only possible because we have accounted for v_0 in our definitions of the geomorphic length, height, and timescales ℓ_g , h_g , and t_g . We noted previously there that we are free to choose a value of v_0 , as there will always be a corresponding value of k_w to satisfy the relationship between w and a . What then is a physically meaningful characteristic contour width, and how would we identify it outside of the context of a landscape evolution model? One possible explanation appears in the hydromorphic balance equation (62) for the upslope area at channel heads, A_c . Here the characteristic contour width appears in the numerator $v_0 b k_s$, which is effectively the transmissivity integrated across a characteristic contour width. This integrated transmissivity is particularly important at channel heads, where relative magnitudes of surface and subsurface flow are similar. Upstream of the channel head, the contour width is less important, as topographic features do not constrict groundwater flow to a fixed width. Further downstream from the channel head, groundwater flow is constricted by the valley width, but most of the discharge will be transmitted as surface water rather than groundwater. Because A_c scales with v_0 just as it does with the transmissivity $b k_s$, v_0 plays a critical role in determining the extent of landscape dissection, as increasing channel head source areas increases the distance from channels to ridges. In landscapes similar to those modeled here, we suggest that the characteristic contour width is best thought of as characteristic channel head width, and that more attention should be paid to this factor in field investigations.

1006 **7.5 Landscape complexity**

1007 In developing this first systematic exploration of the effects of subsurface flow on
 1008 steady-state landscape form, we have neglected the complexity of landscape processes
 1009 and heterogeneity of landscape properties in favor of an approach with a tractable num-
 1010 ber of parameters so that we can explore the diversity of behaviors it can produce. How-
 1011 ever, it is likely that processes and heterogeneity not captured here have significant im-
 1012 pacts on landscape form. Subsurface properties are not only heterogeneous, but spatially
 1013 organized, including systematic variations in permeability with depth through soil and
 1014 weathered bedrock and along hillslope catenas (Lohse & Dietrich, 2005). The scope of
 1015 runoff generation processes we have examined is also limited, as we have not considered
 1016 infiltration excess overland flow, nor other erosional processes that are linked to shallow
 1017 groundwater, including seepage erosion (Abrams et al., 2009; Laity & Malin, 1985) and
 1018 landsliding driven by excess pore water pressure (Montgomery & Dietrich, 1994). Like-
 1019 wise, ecological processes may act on the environment in ways that cannot be captured
 1020 by the processes and parameters included here. For example, feedback between depth
 1021 to water-table and tree growth may affect spatial patterns of hillslope and fluvial sed-
 1022 iment transport, as trees anchor sediment with roots, displace sediment through treethrow,
 1023 or encourage soil production (Brantley, Eissenstat, et al., 2017; Gabet & Mudd, 2010).

1024 **7.6 Steady-state topography**

1025 In this study we have focused on evaluating landscapes near topographic steady-
 1026 state in order to understand the emergent relationships between topography and hydrolog-
 1027 ogy generated by these governing equations. This is a powerful method employed in land-
 1028 scape evolution models to understand the form toward which landscapes will evolve (e.g.,
 1029 Perron et al., 2008; Theodoratos et al., 2018). In the model we have used here, however,
 1030 times to steady-state are long (millions to tens of millions of years) compared to real timescales
 1031 of variability in climate and baselevel change. For this reason, transience, at least in some
 1032 portions of the landscape, is likely the norm in real landscapes with similar dominant
 1033 processes to those modeled here (Whipple, 2001). On the other hand, nonlinear mod-
 1034 els of hillslope diffusion show substantially shorter times to steady-state (Roering et al.,
 1035 2001), which may be important when hillslopes are the limiting factor in reaching to-
 1036 polographic steady-state. Further investigation could focus on transient responses the model
 1037 considered here, which may provide insights into a wider range of humid landscapes.

1038 **7.7 Steady recharge**

1039 In this model, we have shown that runoff generation from shallow groundwater driven
 1040 by steady recharge has a strong effect on emergent landscape properties. With increas-
 1041 ing γ , we found that the hydrological function of the landscape was increasingly binary:
 1042 channels have surface runoff nearly equal to the sum of the recharge on the area upslope,
 1043 while hillslopes do not contribute surface runoff at all. While this may be characteris-
 1044 tic of some landscapes where saturated areas are more or less constant in time, in many
 1045 places, saturated areas and wetted channels expand and contract in response to the ar-
 1046 rival of storm events or snow melt (Dunne & Black, 1970; Nippgen et al., 2015; Antonelli
 1047 et al., 2020). Furthermore, antecedent wetness plays an important role in determining
 1048 the hydrological response to precipitation (Longobardi et al., 2003; O'Loughlin, 1981).
 1049 As fluvial sediment transport in our model is proportional to runoff Q^* , we expect that
 1050 precipitation variability and subsurface water storage would affect sediment transport,
 1051 ultimately affecting the landscape form as well. Previous studies have shown that land-
 1052 scape form and channel profiles have are sensitive to variability in precipitation or dis-
 1053 charge, depending on factors including the presence of erosion thresholds and the non-
 1054 linearity of the fluvial incision model (Tucker, 2004; Lague et al., 2005; Deal et al., 2018).
 1055 In a future contribution, we will extend the theoretical framework used here to incor-

1056 porate stochastic precipitation, allowing us to explore the emergence of hydrogeomor-
 1057 phic features such as variable source areas.

1058 8 Conclusion

1059 Here we have coupled a model of shallow groundwater flow with a model of denuda-
 1060 tional landscape evolution, and have shown the first results of such a model at topographic
 1061 steady-state. The shallow aquifer model uses the Dupuit-Forcheimer assumptions to gen-
 1062 erate lateral groundwater flow and surface water discharge from groundwater return flow
 1063 and precipitation on saturated areas. The topography evolves according to fluvial inci-
 1064 sion by runoff generated by the groundwater model, linear hillslope diffusion, and a con-
 1065 stant rate of uplift. We use a novel scaling analysis to guide our numerical simulations,
 1066 and find that the subsurface drainage capacity relative to climate plays a critical role in
 1067 setting topographic properties including hillslope length. We showed that the linear re-
 1068 lationship between steepness and Laplacian curvature that emerges from the simple stream-
 1069 power incision-linear diffusion LEM bifurcates with increasing subsurface drainage ca-
 1070 pacity: saturated areas tend toward the linear relationship between steepness and cur-
 1071 vature, while unsaturated hillslopes maintain constant negative curvature regardless of
 1072 steepness. By incorporating the steady-state solution of the hydrological model, we find
 1073 that every point in topography lies near a manifold that relates steepness, Laplacian cur-
 1074 vature, and topographic index. This contrasts with the simpler linear relationship be-
 1075 tween steepness and curvature in the absence of runoff generation from the shallow sub-
 1076 surface. A complementary analysis of the governing equations at steady-state showed
 1077 that hillslope length should scale with the subsurface drainage capacity, and therefore
 1078 the transmissivity, to the power 2/3. This was supported by our numerical results for
 1079 sufficiently large drainage capacities. Links between landscape form and hydrologic func-
 1080 tion have been long sought-after in hydrology. By analyzing these interactions in an ide-
 1081 alized model framework, we have demonstrated the potential for subsurface hydrologic
 1082 properties to profoundly influence surface morphology. However, it remains extremely
 1083 challenging to test whether the predictions of this model are (in detail) representative
 1084 of real landscapes.

1085 9 Notation

1086 Variable definitions are below, with dimensions length L, time T, and mass M. Prime
 1087 always indicates the dimensionless equivalent, where dimensionless equivalents are de-
 1088 fined in the text.

variable	name	dimension
x, y	horizontal coordinates	[L]
t	time	[T]
$z(x, y)$	topographic elevation	[L]
$h(x, y)$	aquifer thickness	[L]
$A(x, y)$	area upslope	[L ²]
$a(x, y)$	area upslope per unit contour width	[L]
$\theta(x, y)$	aquifer base slope angle	[rad]
h_g	characteristic geomorphic height scale	[L]
ℓ_g	characteristic geomorphic length scale	[L]
t_g	characteristic geomorphic time scale	[T]
h_a	characteristic aquifer thickness	[L]
t_d	characteristic time to drain aquifer storage	[T]
δ	timescale factor	[−]
α	characteristic gradient	[−]
γ	drainage capacity	[−]
Hi	hillslope number	[−]
E_f	fluvial incision rate	[L/T]
E_h	hillslope diffusion rate	[L/T]
U	uplift rate	[L/T]
K	streampower incision coefficient	[1/T]
m	streampower area exponent	[−]
n	streampower slope exponent	[−]
v_0	characteristic contour width	[L]
τ	bed shear stress	[M/LT ²]
τ_c	critical bed shear stress	[M/LT ²]
k_e	erosivity coefficient	[M ^{−β} L ^{1+β} T ^{2β−1}]
β	shear stress exponent	[−]
ρ_w	density of water	[M/L ³]
g	acceleration due to gravity	[L/T ²]
d_f	channel flow depth	[L]
C	Chezy coefficient	[L ^{1/2} /T]
w	channel width	[L]
k_w	width coefficient	[−]
b	permeable thickness	[L]
q_h	hillslope sediment transport rate	[L ² /T]
D	hillslope diffusivity	[L ² /T]
k_{sf}	timestep scaling factor	[−]
$q(x, y, t)$	groundwater specific-discharge	[L ² /T]
$q_s(x, y, t)$	local surface runoff	[L/T]
$Q(x, y, t)$	discharge	[L ³ /T]
$Q^*(x, y, t)$	dimensionless discharge	[−]
p	recharge rate	[L/T]
k_s	hydraulic conductivity	[L/T]
n_e	drainable porosity	[−]
\mathcal{G}	step function	[−]
\mathcal{R}	ramp function	[−]
a_c	critical area per contour width	[L]
A_c	critical area	[L ²]
L_h	mean hillslope length	[L]

Accepted Article

Appendices

A DupuitLEM dimensionless equations from symmetry groups

Here we extend the scaling analysis applied to the *NoHyd* model to include the governing hydrological equations in the *DupuitLEM* model. Because the hydrological model is linked to the geomorphic model through Q^* , the set of transformations used for the geomorphic equations above is not necessarily applicable to the *DupuitLEM* model. In addition to the characteristic scales ℓ_g , h_g , and t_g used for the *NoHyd* model, we will introduce two scales particularly relevant to hydrological processes: a characteristic aquifer thickness h_a and a characteristic aquifer drainage time t_d . First we derive these quantities. A simple mass balance of water in a 1D hillslope with length ℓ_g , relief h_g , recharge rate p , and hydraulic conductivity k_s gives:

$$p\ell_g = h_a k_s h_g / \ell_g. \quad (\text{A1})$$

It is worth noting that because topography and hydrology evolve together in our model, we do not know what the actual mean hillslope length and relief will be. Nonetheless, incorporating h_g and ℓ_g as characteristic hillslope scales allows us to capture some dependence of emergent topographic properties on underlying geomorphic processes. The characteristic drainage time for a shallow aquifer can be derived from Harman and Sivapalan (2009, their eq. 6), which likewise describes the drainage of an aquifer with characteristic length and relief with drainable porosity n_e :

$$t_d = \frac{\ell_g n_e}{k_s \sin \theta} \quad (\text{A2})$$

Making the approximation $\sin(\theta) \sim h_g/\ell_g$, the resulting characteristic scales are:

$$h_a = \frac{p\ell_g}{k_s h_g / \ell_g} \quad (\text{A3})$$

$$t_d = \frac{\ell_g n_e}{k_s h_g / \ell_g} \quad (\text{A4})$$

In addition to the recast landscape evolution equations in (20) and (21), we add those of the hydrological model, replacing parameters with equivalent combinations of the characteristic scales:

$$\frac{\partial h}{\partial t} = \frac{h_a}{t_d} \left(1 - \frac{\nabla \cdot q}{p} - \frac{q_s}{p} \right) \quad (\text{A5})$$

$$\frac{q}{p} = -h \cos^2(\arctan |\nabla z|) \frac{\ell_g^2}{h_g h_a} (\nabla h + \nabla z) \quad (\text{A6})$$

$$\frac{q_s}{p} = \mathcal{G}\left(\frac{h}{b}\right) \mathcal{R}\left(1 - \frac{\nabla \cdot q}{p}\right) \quad (\text{A7})$$

$$Q^* = \frac{1}{Ap} \int_A q_s dA_c \quad (\text{A8})$$

Here we have expanded the aquifer base angle $\theta = \arctan |\nabla z_b| = \arctan |\nabla z|$, as constant permeable thickness implies that the aquifer base gradient is equal to the topographic gradient. As with the scaling analysis in equations (20) and (21), we can look for sets of transformations under which the equations are invariant. The symmetry group for the time dimension shown in (28) will apply as before. However we can-

not separately transform the vertical and horizontal length scales in the hydrologic equations. This is because we cannot cancel a scaling factor on ∇ in the cosine term of (A6) without scaling z as well, and vice versa. As a result, horizontal and vertical dimensions must be transformed together, leaving only two symmetry groups that produce invariance:

$$\begin{aligned} & \{t \rightarrow ct, t_g \rightarrow ct_g, t_d \rightarrow ct_d\} \\ & \{x \rightarrow cx, y \rightarrow cy, a \rightarrow ca, A \rightarrow c^2 A, l_g \rightarrow cl_g, \\ & \quad q \rightarrow cq, z \rightarrow cz, h \rightarrow ch, h_g \rightarrow ch_g, h_a \rightarrow ch_a, b \rightarrow cb\} \end{aligned} \quad (\text{A9})$$

Again, we can choose particular values for scaling factors c and apply the transformations in the symmetry groups in search of a form that eliminates or consolidates the characteristic scales. We will first apply the time symmetry group, choosing $c = 1/(t_g t_d)$. This is equivalent to applying the transformations in the group twice, once with $c = 1/t_g$ and again with $c = 1/t_d$. We will then apply the second group, choosing $c = 1/(\ell_g h_g h_a)$. Likewise, this is equivalent to applying it three times with each of the three factors in the denominator. Applying these scales, we obtain the dimensionless form of the hydrological equations, presented in the main text, Equations (35)-(40).

B Scaling analysis in special cases

The governing hydrological equations account for the effects of gradients in aquifer thickness and gradients in aquifer base elevation in driving groundwater flow. These equations can be simplified under conditions where one gradient is more important than the other, reducing the constraints on our symmetry groups. Suppose that topographic gradients are generally insignificant, and groundwater flow is driven by gradients in aquifer thickness ($\nabla h \gg \nabla z$). In this case, the expression for groundwater specific-discharge changes again, as we can approximate $\cos \theta \approx 1$ and $\nabla z \approx 0$ for the purposes of groundwater flow. Then the governing equations are again the same except for q :

$$\frac{q}{p} = -h \frac{\ell_g^2}{h_g h_a} \nabla h \quad (\text{B1})$$

In this case, because the cosine term does not appear, ℓ_g and h_g need not be scaled together, as discussed in Appendix A. There are now three transformations that maintain symmetry. Namely we no longer need to scale horizontal and vertical dimensions together, but we do need scale to aquifer thickness h with the vertical scales in order to maintain consistency in the groundwater specific-discharge equation.

$$\begin{aligned} & \{t \rightarrow ct, t_g \rightarrow ct_g, t_d \rightarrow ct_d\} \\ & \{h \rightarrow ch, h_a \rightarrow ch_a, b \rightarrow cb, z \rightarrow cz, h_g \rightarrow ch_g\} \\ & \{x \rightarrow cx, y \rightarrow cy, a \rightarrow ca, A \rightarrow c^2 A, l_g \rightarrow cl_g, q \rightarrow cq\} \end{aligned} \quad (\text{B2})$$

Noting the similarities with the transformation of the full *DupuitLEM* model, we select the scales $c = 1/(t_g t_d)$, $c = 1/(h_a h_g)$, and $c = 1/\ell_g$ respectively. We arrive at a rescaled set of governing equations for the case in which flow is primarily driven by gradients in aquifer thickness. The result is the same as Equations (35)-(40), except that the equation for q' (38) has changed to

$$q' = -h' \frac{\nabla' h'}{\text{Hi}}. \quad (\text{B3})$$

Under these conditions, the hillslope number $\text{Hi} = h_g/h_a$ still appears in the ground-water specific-discharge expression, while the characteristic gradient $\alpha = h_g/\ell_g$ no longer appears. This suggests that as Hi becomes small, the sensitivity to Hi does not decrease, but sensitivity to α does decrease. Small Hi indicates that water-table gradients are more important than topographic gradients in driving flow. As α is an indicator of topographic gradients, it is appropriate that it should diminish in importance when Hi is small.

Conversely, suppose that relief is generally large in comparison to aquifer thickness, $h_g \gg h_a$, in which case the hillslope number $\text{Hi} \gg 1$. Consequently, topographic gradients rather than aquifer thickness gradients tend to drive groundwater flow. In this case we neglect ∇h , altering the groundwater specific-discharge expression (A6) to

$$\frac{q}{p} = -h \cos^2(\arctan |\nabla z|) \frac{\ell_g^2}{h_g h_a} \nabla z. \quad (\text{B4})$$

Applying our symmetry method as before, we find that ℓ_g and h_g must still be scaled together. However, this time, aquifer thickness h need not be scaled with these simultaneously in order to obtain a consistent set of equations. Instead, there are now three sets of transformations that comprise the symmetry:

$$\begin{aligned} & \{t \rightarrow ct, t_g \rightarrow ct_g, t_d \rightarrow ct_d\} \\ & \{h \rightarrow ch, h_a \rightarrow ch_a, b \rightarrow cb\} \\ & \{x \rightarrow cx, y \rightarrow cy, a \rightarrow ca, A \rightarrow c^2 A, l_g \rightarrow cl_g, \\ & \quad q \rightarrow cq, z \rightarrow cz, h_g \rightarrow ch_g\} \end{aligned} \quad (\text{B5})$$

Implementing the three transformations above with $c = 1/(t_g t_d)$, $c = 1/h_a$, and $c = 1/(h_g \ell_g)$ respectively, we arrive at a rescaled set of governing equations the same as those found in Equations (35)-(40), only with an altered expression for q' :

$$q' = -h' \cos^2(\arctan |\nabla' z' h_g / \ell_g|) \nabla' z' \quad (\text{B6})$$

Here the hillslope number Hi no longer appears in the equation. This suggests that the solution to the full governing equations should be independent of Hi when Hi is large. This makes sense in the context of Equation (38), as $1/\text{Hi}$ multiplies the gradient in aquifer thickness, which should be small relative to topographic gradients when Hi is large.

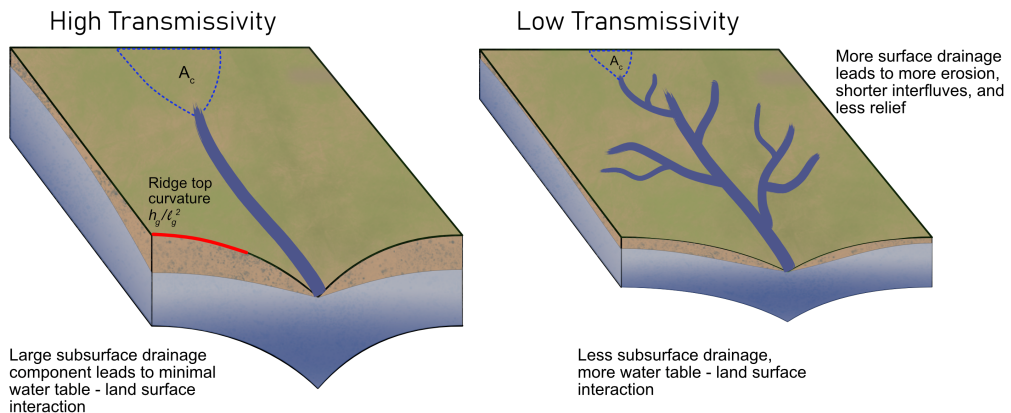


Figure 1. Illustration of two landscapes showing hypothesized differences in morphology with subsurface transmissivity given same geologic and climatic setting. The lower transmissivity landscape (right) transports less water through the subsurface, and therefore has smaller subsurface contributing areas before flow emerges at the surface. The greater extent of surface flow results in greater dissection, as reflected in the development of a denser drainage network with lower-relief interfluves.

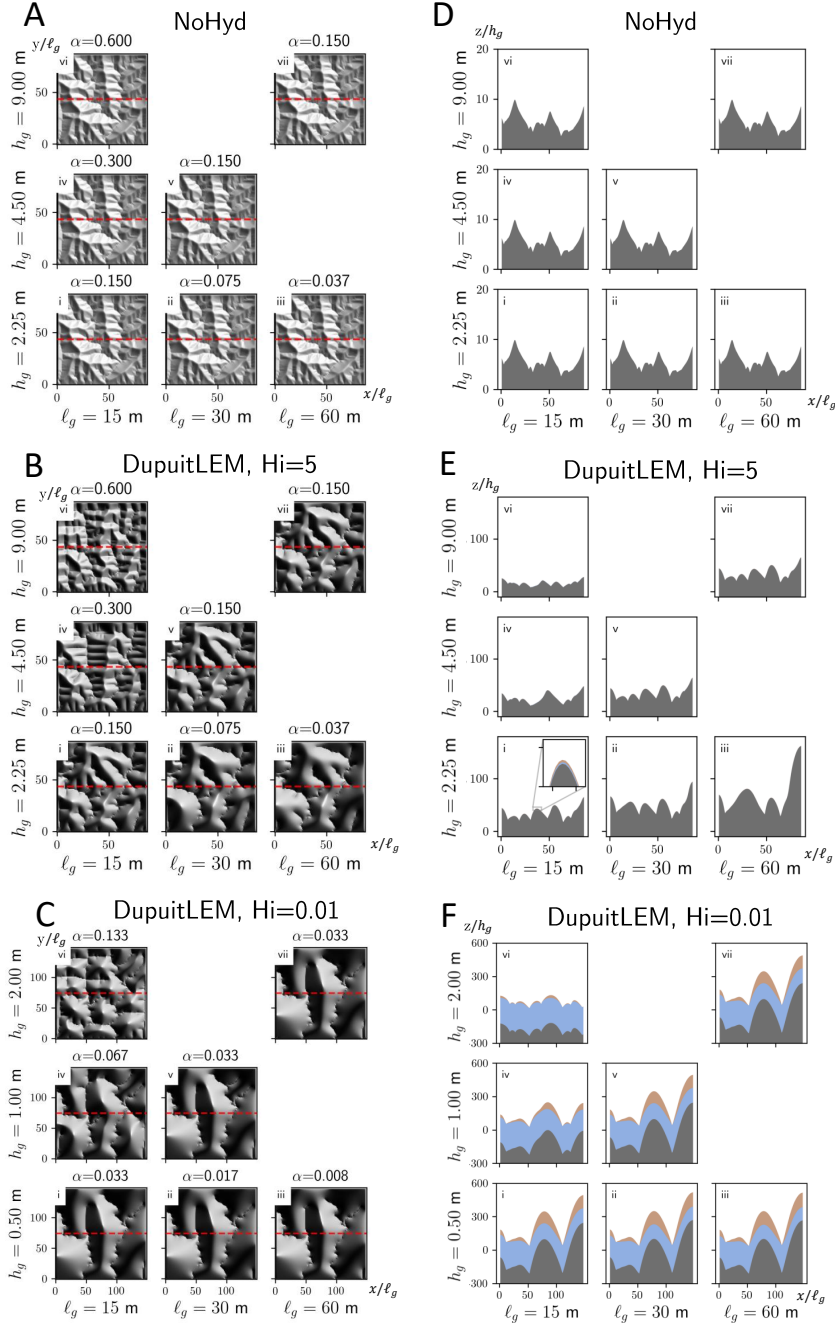


Figure 2. Hillshade plots (A, B, C) and cross-sections (D, E, F) of steady-state elevation for model runs with varying h_g and ℓ_g . Cross-sections are taken along the dashed red lines. Data plotted are in the re-scaled coordinate system (x', y', z') . (A, D) Model runs with the *NoHyd* model, showing topography is nearly identical between the runs in the dimensionless coordinate system regardless of the chosen values of h_g and ℓ_g . (B, E) *DupuitLEM* model results are sensitive to independent scaling of ℓ_g ($i \rightarrow ii \rightarrow iii$) and h_g ($i \rightarrow iv \rightarrow vi$) when Hi is large. Scaling such that $\alpha = h_g/\ell_g$ remains constant produces topography that is similar in the re-scaled coordinates. (C, F) *DupuitLEM* results with small Hi , showing reduced sensitivity of modeled topography to chosen length scales for small values of α . Note that the dimensionless size of the domain in the $Hi = 0.01$ cases is larger than the other cases in order to resolve a sufficient number of ridge-valley features. This was accomplished by maintaining the number of grid cells and increasing the contour width v_0 . The values of h_g in the $Hi = 0.01$ cases (C, F) are also smaller to allow for achievement of a tractable solution with very small Hi . Cross-sections show zero elevation (blue), and topographic elevation boundary condition along the lower edge of the domain.

Accepted Article

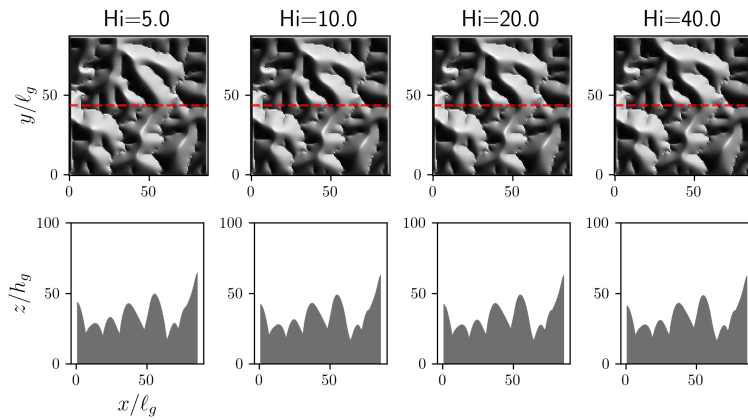


Figure 3. Hillshade and cross-sections of steady-state elevation from *DupuitLEM* for large values of Hi , with $\alpha = 0.15$ and $\gamma = 2.5$. cross-sections are taken along the dashed red lines and domain scaled in same fashion as 2. Results confirm that model topography is insensitive to Hi at large values of Hi , as predicted by the scaling analysis.

Accepted Article

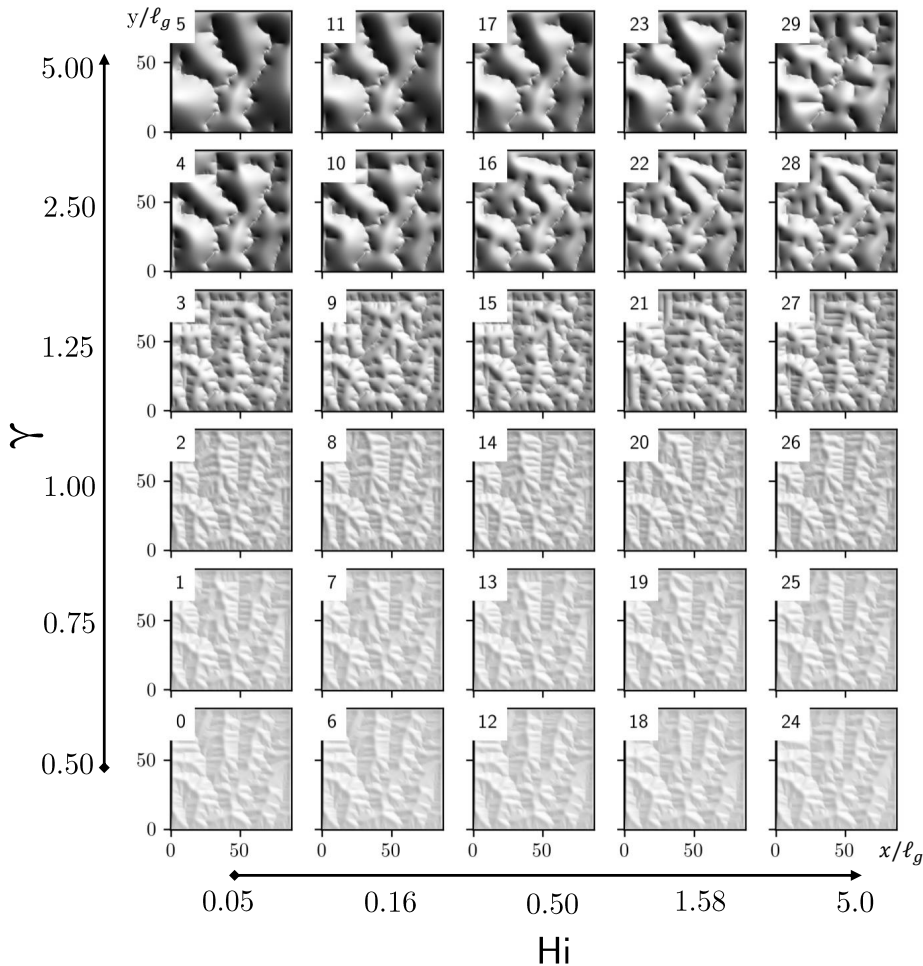


Figure 4. Hillshade plots of steady-state elevation using the *DupuitLEM* model varying γ and Hi while α is held constant. Hi varies over two orders of magnitude on a geometric scale, while γ varies over one order of magnitude, further subdivided to show the transition that occurs at $\gamma = 1$. Low γ topography appears similar to *NoHyd* model results, and is less sensitive to varying Hi . Large γ results show broad hillslopes and slightly greater sensitivity to Hi .

Accepted Article

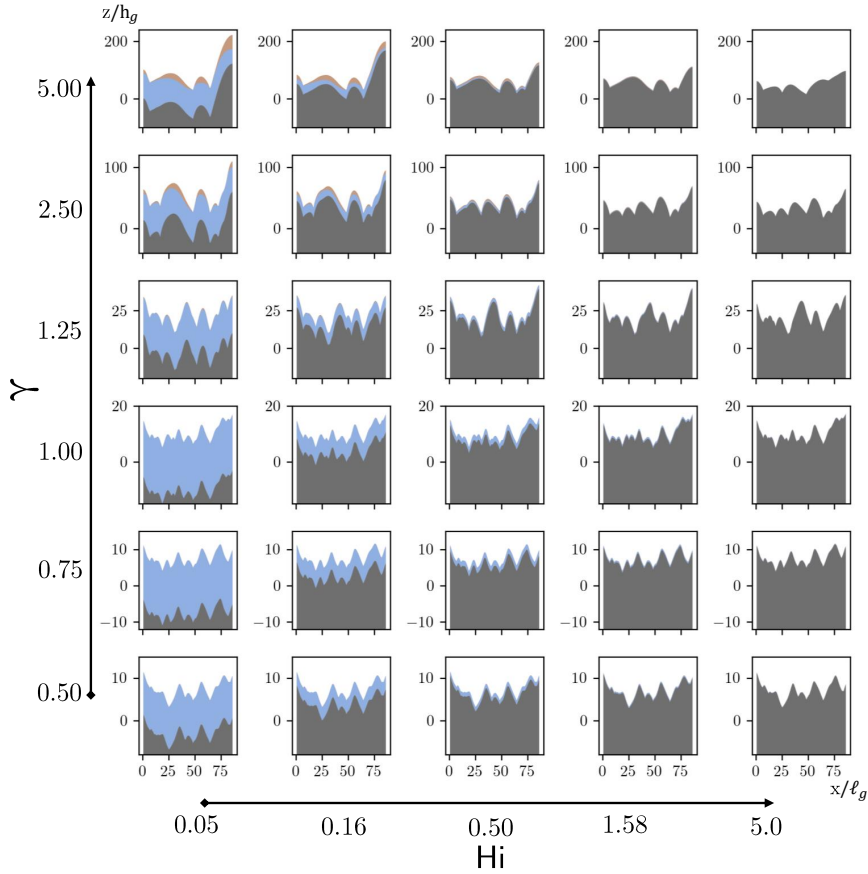


Figure 5. cross-section plots of *DupuitLEM* model results with varying γ and Hi corresponding to hillshades in Figure 4. cross-sections are taken in the same fashion to Figure 2, horizontally along the midpoint of the domain. Despite apparent similarities of the hillshades, there are prominent differences in the subsurface with varying Hi . Lower Hi cases will have deeper regolith, as this is dependent on the value of Hi . Noticeable depth to water-table only becomes apparent at large values of γ .

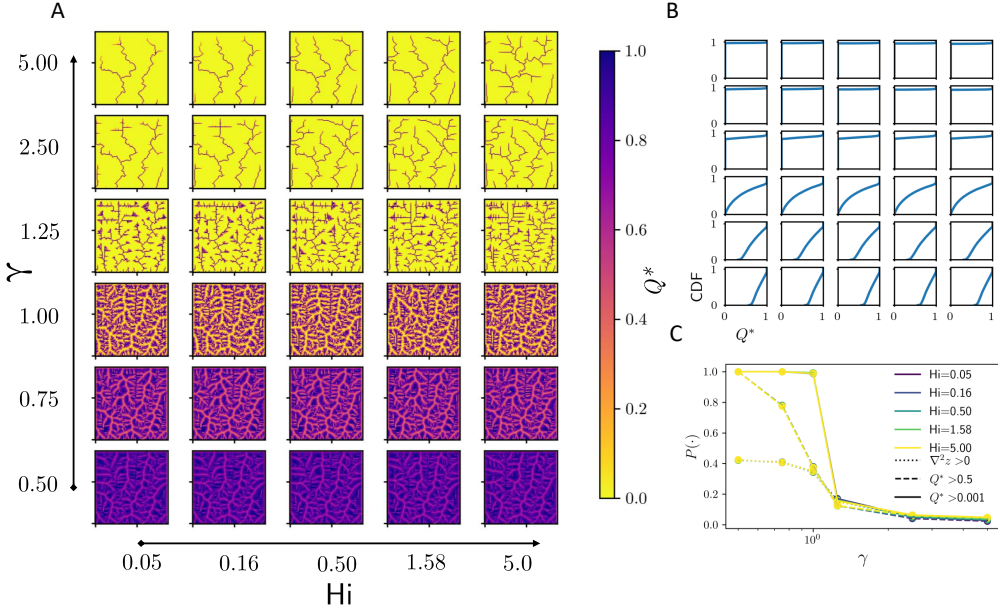


Figure 6. (A) Spatial patterns of Q^* from the *DupuitLEM* model varying γ and Hi while all other parameters are held constant. Results are similar across differences in Hi , but show significant differences with γ . All points in the landscape generate some runoff in the lowest *gamma* trials. (B) Cumulative distribution functions of Q^* with varying γ and Hi . Low γ trials show a range of Q^* values, with all areas contributing to some degree. High γ cases show most areas do not contribute runoff, with a small number where $Q^* \approx 1$. (C) Proportion of nodes contributing runoff at $Q^* > 0.5$, with varying γ (x-axis) and Hi (colors). Extent of areas contributing runoff is small for large Hi , and generally decreases with decreasing Hi .

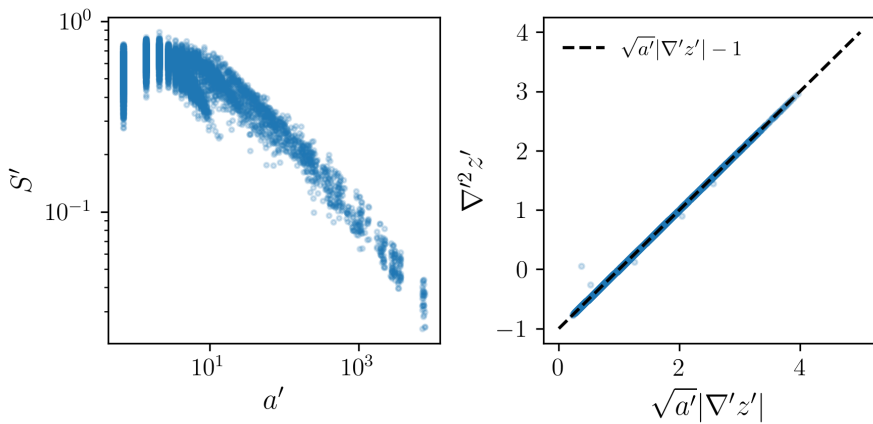


Figure 7. Dimensionless slope-area (left) and steepness-curvature plots (right) of steady-state topography using the *NoHyd* model. Area per contour width is used in place of area in both plots to maintain consistency with model formulation. The steepness-curvature relationship observed in the data show a precise fit to the linear relationship predicted from theory (dotted line). Parameters selected are the same as Figure 2Ai.

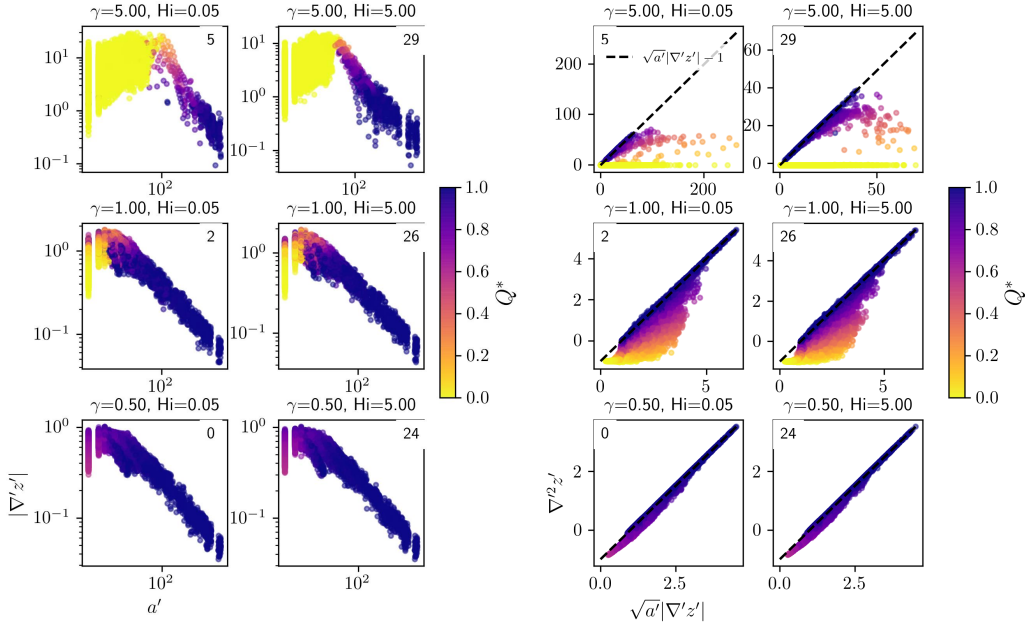


Figure 8. Dimensionless slope-area (left) and steepness-curvature (right) plots for selected model runs from Figure 4. See correlating numbers in the upper left corner. As in Figure 4, γ and Hi increase vertically and laterally from the bottom left respectively. Plots are colored by Q^* of the final topography. Axes scales are different between plots, showing that large γ cases obtain values of steepness and curvature far greater than the cases when γ is small.

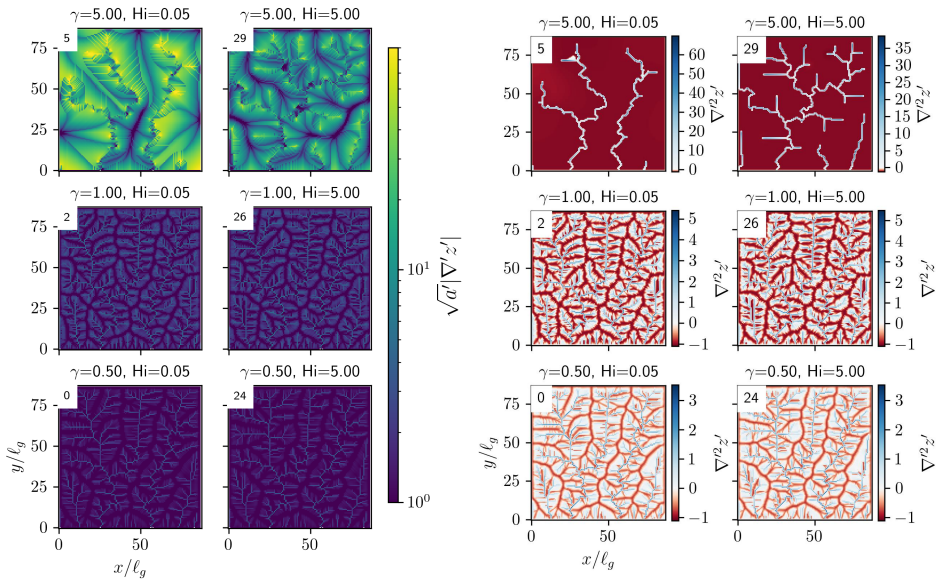


Figure 9. Planform view steepness and curvature for selected model runs, with run number corresponding to hillshades in figure 4. Spatial pattern of steepness appears to agree with channel network locations in the low γ cases, while in the high γ cases, it takes on large values in patterns that spiral away from ridges. Curvature is positive on ridges and negative in channels, with large areas of constant negative curvature in the large γ cases.

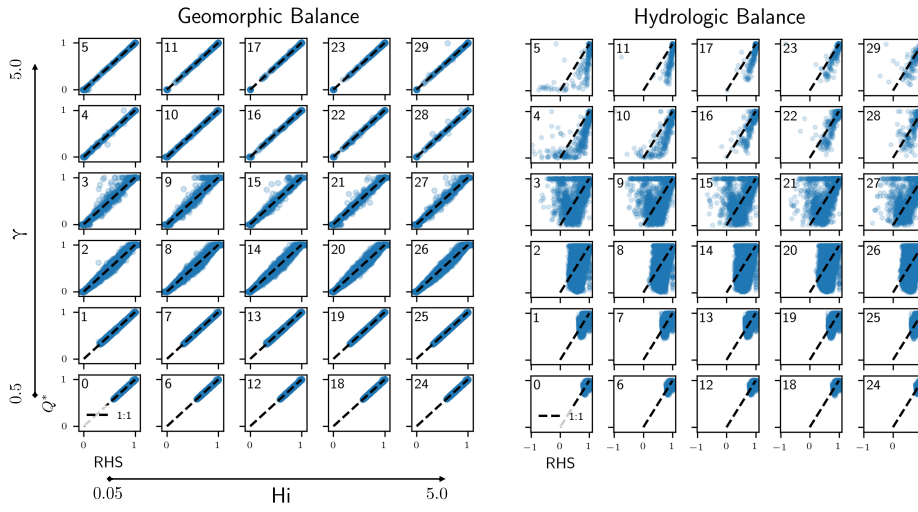


Figure 10. Planform view topographic index (left) and topographic index- Q^* relationship for selected model runs, with run number corresponding to hillshades in figure 4. Coloring in the right panel reveals that curvature explains variation in Q^* at a given topographic index.

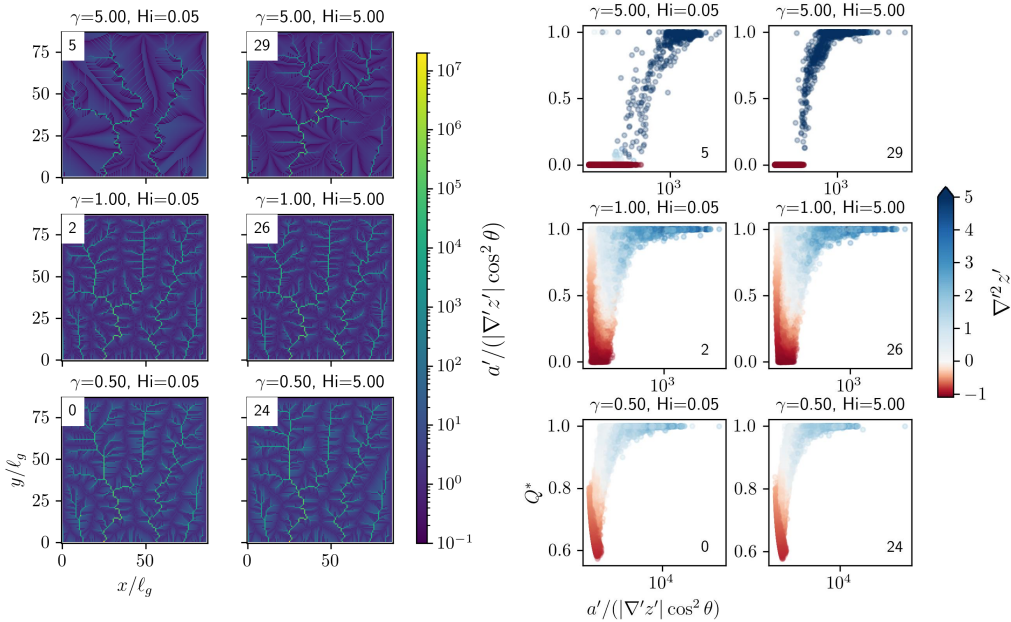


Figure 11. (A) Geomorphic balance from equation (48), plotting Q^* against the right hand side (RHS) of the equation. Subplots correspond to the same model runs as in 4. (B) Hydrologic balance from equation (56), plotting Q^* against the right hand side of the equation.

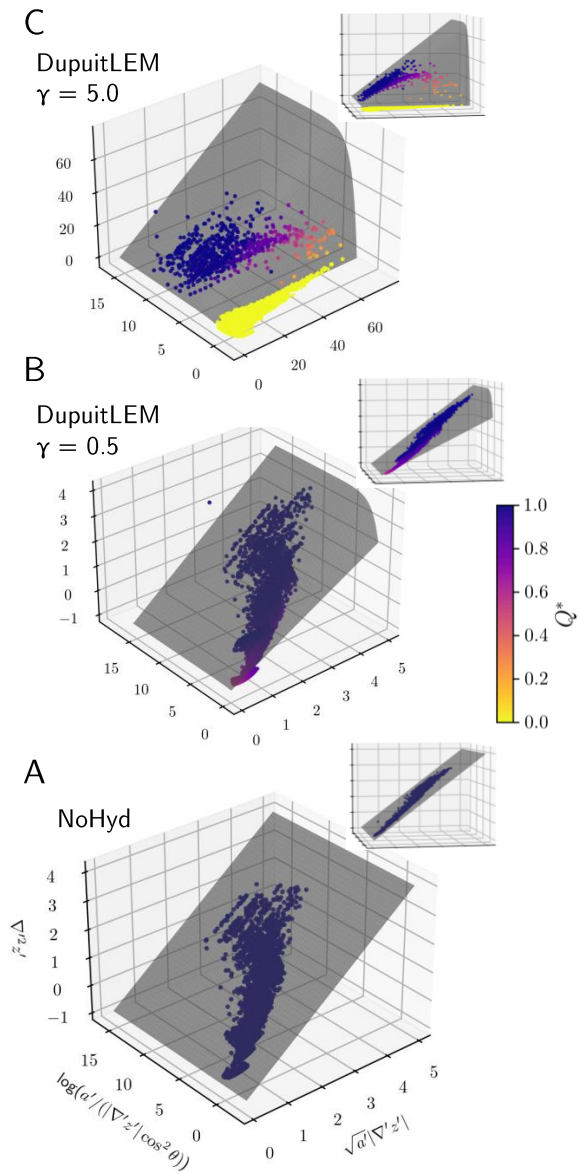


Figure 12. Plots of the manifold (grey) defined in equation (59) and topography colored by Q^* showing how the form of the solution varies with γ . Both (B) and (C) have $Hi = 5.0$. Inset figures show the same results rotated 30 degrees to emphasize how the solution compares to the steepness-curvature relationship.

Accepted Article

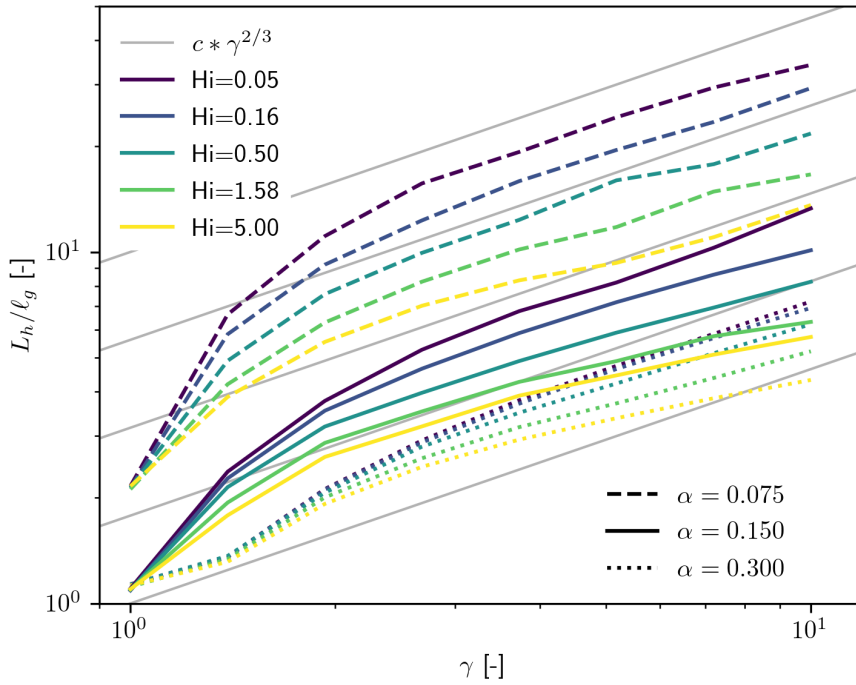


Figure 13. Hillslope length L_h increases with increasing γ . For a value of γ and α , L_h increases with decreasing Hi . Similarly, for a given value of γ and Hi , L_h increases with decreasing α . Gray lines with varying coefficients c show that the hillslope length scales approximately as $\gamma^{2/3}$ for $\gamma > 1$, which we derive from the hydromorphic balance.

1167 **Acknowledgments**

1168 This work was supported by NSF grants EAR-2012264, EAR-1654194, ACI-1450409, EAR-
 1169 1725774, and EAR-1831623. The authors would like to thank Clement Roques and two
 1170 anonymous reviewers for their comments which have significantly improved the manuscript.
 1171 No original data is presented in this paper. The Python package DupuitLEM v1.0 (D. G. Litwin
 1172 et al., 2021) contains the models and scripts used to generate output, post-process out-
 1173 put, and create figures presented here. Landlab v2.0 (Hutton et al., 2020) is a core de-
 1174 pendency of DupuitLEM, while NumPy (Harris et al., 2020), Pandas (pandas develop-
 1175 ment team, 2020), and Matplotlib (Hunter, 2007) were used for additional analysis and
 1176 visualization. The complete list of input parameter values can be found in Table S1.

1177 **References**

- 1178 Abrams, D. M., Lobkovsky, A. E., Petroff, A. P., Straub, K. M., McElroy, B.,
 1179 Mohrig, D. C., ... Rothman, D. H. (2009). Growth laws for channel net-
 1180 works incised by groundwater flow. *Nature Geoscience*, 2(3), 193–196. doi:
 1181 10.1038/ngeo432
- 1182 Ahnert, F. (1976). Brief description of a comprehensive three-dimensional process-
 1183 response model of landform development. *Zeitschrift fr Geomorphologie, Sup-*
 1184 *plement*, 25, 29–49.
- 1185 Antonelli, M., Glaser, B., Teuling, A. J., Klaus, J., & Pfister, L. (2020). Saturated
 1186 areas through the lens: 1. Spatiotemporal variability of surface saturation doc-
 1187 umented through thermal infrared imagery. *Hydrological Processes*, 34(6),
 1188 1310–1332. doi: 10.1002/hyp.13698
- 1189 Armstrong, A. (1976). A three-dimensional simulation of slope forms. *Zeitschrift fr*
 1190 *Geomorphologie, Supplement*, 25, 20–28.
- 1191 Barenblatt, G. I. (1996). *Scaling, self-similarity, and intermediate asymptotics*
 1192 (No. 14). Cambridge ; New York: Cambridge University Press.
- 1193 Barnhart, K. R., Hutton, E. W. H., Tucker, G. E., Gasparini, N. M., Istanbullu-
 1194 oglu, E., Hobley, D. E. J., ... Bandaragoda, C. (2020). Short communica-
 1195 tion: Landlab v2.0: a software package for Earth surface dynamics. *Earth*
 1196 *Surface Dynamics*, 8(2), 379–397. (Publisher: Copernicus GmbH) doi:
 1197 <https://doi.org/10.5194/esurf-8-379-2020>
- 1198 Barnhart, K. R., Tucker, G. E., Doty, S. G., Glade, R. C., Shobe, C. M., Rossi,
 1199 M. W., & Hill, M. C. (2020). Projections of Landscape Evolution on a
 1200 10,000 Year Timescale With Assessment and Partitioning of Uncertainty
 1201 Sources. *Journal of Geophysical Research: Earth Surface*, 125(12). doi:
 1202 <https://doi.org/10.1029/2020JF005795>
- 1203 Barnhart, K. R., Tucker, G. E., Doty, S. G., Shobe, C. M., Glade, R. C., Rossi,
 1204 M. W., & Hill, M. C. (2020). Inverting Topography for Landscape Evolu-
 1205 tion Model Process Representation: 3. Determining Parameter Ranges for
 1206 Select Mature Geomorphic Transport Laws and Connecting Changes in Fluvial
 1207 Erodibility to Changes in Climate. *Journal of Geophysical Research: Earth*
 1208 *Surface*, 125(7), e2019JF005287. doi: 10.1029/2019JF005287
- 1209 Berne, A., Uijlenhoet, R., & Troch, P. A. (2005). Similarity analysis of subsurface
 1210 flow response of hillslopes with complex geometry. *Water Resources Research*,
 1211 41(9), 1–10. doi: 10.1029/2004WR003629
- 1212 Beven, K. J., & Kirkby, M. J. (1979). A physically based, variable contributing area
 1213 model of basin hydrology. *Hydrological Sciences Bulletin*, 24(1), 43–69. (ISBN:
 1214 0262666790) doi: 10.1080/02626667909491834
- 1215 Bishop, P. (2007). Long-term landscape evolution: linking tectonics and surface pro-
 1216 cesses. *Earth Surface Processes and Landforms*, 32(3), 329–365. doi: <https://doi.org/10.1002/esp.1493>
- 1217 Bonetti, S., Bragg, A. D., & Porporato, A. (2018). On the theory of drainage area
 1218 for regular and non-regular points. *Proceedings of the Royal Society A: Mathe-*

- matical, Physical and Engineering Sciences*, 474(2211), 20170693. (Publisher: Royal Society) doi: 10.1098/rspa.2017.0693

Bonetti, S., Hooshyar, M., Camporeale, C., & Porporato, A. (2020). Channelization cascade in landscape evolution. *Proceedings of the National Academy of Sciences*, 117(3), 1375–1382. (Publisher: National Academy of Sciences) doi: 10.1073/pnas.1911817117

Brantley, S. L., Eissenstat, D. M., Marshall, J. A., Godsey, S. E., Balogh-Brunstad, Z., Karwan, D. L., ... Weathers, K. C. (2017). Reviews and syntheses: On the roles trees play in building and plumbing the critical zone. *Biogeosciences*, 14(22), 5115–5142. doi: 10.5194/bg-14-5115-2017

Brantley, S. L., Lebedeva, M. I., Balashov, V. N., Singha, K., Sullivan, P. L., & Stinchcomb, G. (2017). Toward a conceptual model relating chemical reaction fronts to water flow paths in hills. *Geomorphology*, 277, 100–117. doi: 10.1016/j.geomorph.2016.09.027

Braun, J., & Willett, S. D. (2013). A very efficient O(n), implicit and parallel method to solve the stream power equation governing fluvial incision and landscape evolution. *Geomorphology*, 180–181, 170–179. doi: 10.1016/j.geomorph.2012.10.008

Bresciani, E., Davy, P., & de Dreuzy, J.-R. (2014). Is the Dupuit assumption suitable for predicting the groundwater seepage area in hillslopes? *Water Resources Research*, 50(3), 2394–2406. (Publisher: John Wiley & Sons, Ltd) doi: 10.1002/2013WR014284

Brocca, L., Melone, F., Moramarco, T., & Singh, V. P. (2009). Assimilation of Observed Soil Moisture Data in Storm Rainfall-Runoff Modeling. *Journal of Hydrologic Engineering*, 14(2), 153–165. doi: 10.1061/(ASCE)1084-0699(2009)14:2(153)

Brutsaert, W. (2005). *Hydrology: An Introduction*. Cambridge University Press. Retrieved from https://books.google.com/books?id=yX__xS55xxyoC

Carlston, C. W. (1963). *Drainage density and streamflow*. U.S. Govt. Print. Off. (Google-Books-ID: FLsvAAAAYAAJ)

Chen, A., Darbon, J., & Morel, J.-M. (2014). Landscape evolution models: A review of their fundamental equations. *Geomorphology*, 219, 68–86. doi: 10.1016/j.geomorph.2014.04.037

Childs, E. C. (1971). Drainage of Groundwater Resting on a Sloping Bed. *Water Resources Research*, 7(5), 1256–1263. doi: 10.1029/WR007i005p01256

Deal, E., Braun, J., & Botter, G. (2018). Understanding the Role of Rainfall and Hydrology in Determining Fluvial Erosion Efficiency. *Journal of Geophysical Research: Earth Surface*, 123(4), 744–778. doi: 10.1002/2017JF004393

Dietrich, W. E., Bellugi, D. G., Sklar, L. S., Stock, J. D., Heimsath, A. M., & Roering, J. J. (2003). Geomorphic Transport Laws for Predicting Landscape form and Dynamics. In P. R. Wilcock & R. M. Iverson (Eds.), *Geophysical Monograph Series* (pp. 103–132). Washington, D. C: American Geophysical Union. Retrieved 2021-02-09, from <http://doi.wiley.com/10.1029/135GM09> doi: 10.1029/135GM09

Dietrich, W. E., Wilson, C. J., Montgomery, D. R., & McKean, J. (1993). Analysis of Erosion Thresholds, Channel Networks, and Landscape Morphology Using a Digital Terrain Model. *The Journal of Geology*, 101(2), 259–278. (Publisher: The University of Chicago Press) doi: 10.1086/648220

Dingman, S. L. (1978). Drainage density and streamflow: A closer look. *Water Resources Research*, 14(6), 1183–1187. doi: 10.1029/WR014i006p01183

Dunne, T. (1978). Field studies of hillslope flow processes. In M. J. Kirkby (Ed.), *Hillslope hydrology*. Chichester ; New York: Wiley.

Dunne, T., & Black, R. D. (1970). Partial Area Contributions to Storm Runoff in a Small New England Watershed. *Water Resources Research*, 6(5), 1296–1311. (ISBN: 0043-1397) doi: 10.1029/WR006i005p01296

- 1275 Forte, A. M., Yanites, B. J., & Whipple, K. X. (2016). Complexities of landscape
 1276 evolution during incision through layered stratigraphy with contrasts in rock
 1277 strength. *Earth Surface Processes and Landforms*, 41(12), 1736–1757. doi:
 1278 10.1002/esp.3947
- 1279 Gabet, E. J., & Mudd, S. M. (2009). A theoretical model coupling chemical weath-
 1280 ering rates with denudation rates. *Geology*, 37(2), 151–154. doi: 10.1130/
 1281 G25270A.1
- 1282 Gabet, E. J., & Mudd, S. M. (2010). Bedrock erosion by root fracture and tree
 1283 throw: A coupled biogeomorphic model to explore the humped soil production
 1284 function and the persistence of hillslope soils. *Journal of Geophysical Research: Earth
 1285 Surface*, 115(F4). doi: 10.1029/2009JF001526
- 1286 Gleeson, T., Moosdorf, N., Hartmann, J., & Beek, L. P. H. v. (2014). A glimpse
 1287 beneath earth's surface: GLobal HYdrogeology MaPS (GLHYMPS) of perme-
 1288 ability and porosity. *Geophysical Research Letters*, 41(11), 3891–3898. doi:
 1289 10.1002/2014GL059856
- 1290 Harman, C. J., & Cosans, C. L. (2019). A low-dimensional model of bedrock weath-
 1291 ering and lateral flow coevolution in hillslopes: 2. Controls on weathering and
 1292 permeability profiles, drainage hydraulics, and solute export pathways. *Hydro-
 1293 logical Processes*(December 2018), 1168–1190. doi: 10.1002/hyp.13385
- 1294 Harman, C. J., & Kim, M. (2019). A low-dimensional model of bedrock weath-
 1295 ering and lateral flow coevolution in hillslopes: 1. Hydraulic theory of re-
 1296 active transport. *Hydrological Processes*, 33(4), 466–475. Retrieved from
 1297 <https://onlinelibrary.wiley.com/doi/pdf/10.1002/hyp.13360> doi:
 1298 10.1002/hyp.13360
- 1299 Harman, C. J., & Sivapalan, M. (2009). A similarity framework to assess controls
 1300 on shallow subsurface flow dynamics in hillslopes. *Water Resources Research*,
 1301 45(1), 1–12. doi: 10.1029/2008WR007067
- 1302 Harman, C. J., & Troch, P. A. (2014). What makes Darwinian hydrology "Dar-
 1303 winian"? Asking a different kind of question about landscapes. *Hydrology and
 1304 Earth System Sciences*, 18(2), 417–433. doi: 10.5194/hess-18-417-2014
- 1305 Harris, C. R., Millman, K. J., van der Walt, S. J., Gommers, R., Virtanen, P., Cour-
 1306 napeau, D., ... Oliphant, T. E. (2020). Array programming with NumPy.
 1307 *Nature*, 585(7825), 357–362. doi: 10.1038/s41586-020-2649-2
- 1308 Hewlett, J. D., & Hibbert, A. R. (1967). Factors affecting the response of small wa-
 1309 tersheds to precipitation in humid areas. In *Int. Symp. Forest Hydrology*. doi:
 1310 10.1177/0309133309338118
- 1311 Hobley, D. E. J., Adams, J. M., Nudurupati, S. S., Hutton, E. W. H., Gasparini,
 1312 N. M., Istanbulluoglu, E., & Tucker, G. E. (2017). Creative computing
 1313 with landlab: an open-source toolkit for building, coupling, and exploring
 1314 two-dimensional numerical models of earth-surface dynamics. *Earth Surface
 1315 Dynamics*, 5(1), 21–46. doi: 10.5194/esurf-5-21-2017
- 1316 Horton, R. E. (1945). Erosional development of streams and their drainage basins;
 1317 hydrophysical approach to quantitative morphology. *GSA Bulletin*, 56(3), 275–
 1318 370. doi: 10.1130/0016-7606(1945)56[275:EDOSAT]2.0.CO;2
- 1319 Howard, A. D. (1994). A detachment-limited model of drainage basin evolution. *Wa-
 1320 ter Resources Research*, 30(7), 2261–2285. doi: 10.1029/94WR00757
- 1321 Howard, A. D., & Kerby, G. (1983). Channel changes in badlands. *GSA Bulletin*,
 1322 94(6), 739–752. Retrieved 2020-01-20, from <https://pubs.geoscienceworld.org/gsabulletin/article/94/6/739/202874/Channel-changes-in-badlands> doi: 10.1130/0016-7606(1983)94(739:CCIB)2.0.CO;2
- 1323 Huang, X., & Niemann, J. D. (2006). Modelling the potential impacts of groundwa-
 1324 ter hydrology on long-term drainage basin evolution. *Earth Surface Processes
 1325 and Landforms*. doi: 10.1002/esp.1369
- 1326 Huang, X., & Niemann, J. D. (2008). How do streamflow generation mechanisms af-
 1327 fect watershed hypsometry? *Earth Surface Processes and Landforms*. doi: 10
 1328

- .1002/esp.1573
- Hunter, J. D. (2007). Matplotlib: A 2d graphics environment. *Computing in Science & Engineering*, 9(3), 90–95. doi: 10.1109/MCSE.2007.55
- Hutton, E., Barnhart, K., Hobley, D., Tucker, G., Nudurupati, S. S., Adams, J., ... Rengers, F. (2020). *landlab/landlab: Mrs. Weasley*. Zenodo. doi: 10.5281/zenodo.3776837
- Ijjsz-Vsquez, E. J., Bras, R. L., & Moglen, G. E. (1992). Sensitivity of a basin evolution model to the nature of runoff production and to initial conditions. *Water Resources Research*, 28(10), 2733–2741. doi: <https://doi.org/10.1029/92WR01561>
- Jefferson, A., Grant, G. E., Lewis, S. L., & Lancaster, S. T. (2010). Coevolution of hydrology and topography on a basalt landscape in the Oregon Cascade Range, USA. *Earth Surface Processes and Landforms*, 35(7), 803–816. doi: 10.1002/esp.1976
- Lague, D., Hovius, N., & Davy, P. (2005). Discharge, discharge variability, and the bedrock channel profile. *Journal of Geophysical Research: Earth Surface*, 110(F4). (Publisher: John Wiley & Sons, Ltd) doi: 10.1029/2004JF000259
- Laity, J. E., & Malin, M. C. (1985). Sapping processes and the development of theater-headed valley networks on the Colorado Plateau. *Geological Society of America Bulletin*, 96, 203–217.
- Lapides, D. A., David, C., Sytsma, A., Dralle, D., & Thompson, S. (2020). Analytical Solutions To Runoff On Hillslopes With Curvature: Numerical And Laboratory Verification. *Hydrological Processes*, hyp.13879. doi: 10.1002/hyp.13879
- Leopold, L. B., & Maddock, T. (1953). *The Hydraulic Geometry of Stream Channels and Some Physiographic Implications*. U.S. Government Printing Office. (Google-Books-ID: 4UGH22BKfdsC)
- Litwin, D., Tucker, G., Barnhart, K., & Harman, C. J. (2020). GroundwaterDupuit-Percolator: A Landlab component for groundwater flow. *Journal of Open Source Software*, 5(46), 1935. doi: 10.21105/joss.01935
- Litwin, D. G., Barnhart, K. R., Tucker, G. E., & Harman, C. J. (2021). *DupuitLEM: groundwater landscape evolution with landlab*. Zenodo. doi: 10.5281/zenodo.5522828
- Lohse, K. A., & Dietrich, W. E. (2005). Contrasting effects of soil development on hydrological properties and flow paths. *Water Resources Research*, 41(12), 1–17. doi: 10.1029/2004WR003403
- Longobardi, A., Villani, P., Grayson, R. B., & Western, A. W. (2003). On the relationship between runoff coefficient and catchment initial conditions. *Modelling and Simulation Society of Australia and New Zealand*, 2(1), 1–6. (ISBN: 1-74052-098-X)
- Luo, W., Jasiewicz, J., Stepinski, T., Wang, J., Xu, C., & Cang, X. (2016). Spatial association between dissection density and environmental factors over the entire conterminous United States. *Geophysical Research Letters*, 43(2), 692–700. doi: 10.1002/2015GL066941
- Manga, M. (1996). Hydrology of Spring-Dominated Streams in the Oregon Cascades. *Water Resources Research*, 32(8), 2435–2439. doi: 10.1029/96WR01238
- Marais, J., de Dreuzy, J. R., & Erhel, J. (2017). Dynamic coupling of subsurface and seepage flows solved within a regularized partition formulation. *Advances in Water Resources*, 109, 94–105. doi: 10.1016/j.advwatres.2017.09.008
- Martin, Y., & Church, M. (2004). Numerical modelling of landscape evolution: geomorphological perspectives. *Progress in Physical Geography: Earth and Environment*, 28(3), 317–339. (Publisher: SAGE Publications Ltd) doi: 10.1191/0309133304pp412ra
- Montgomery, D. R., & Dietrich, W. E. (1994). A physically based model for the

- topographic control on shallow landsliding. *Water Resources Research*, 30(4), 1153–1171. (Publisher: John Wiley & Sons, Ltd) doi: 10.1029/93WR02979
- Nippgen, F., McGlynn, B. L., & Emanuel, R. E. (2015). The spatial and temporal evolution of contributing areas. *Water Resources Research*. doi: 10.1002/2014WR016719
- O'Loughlin, E. M. (1981). Saturation regions in catchments and their relations to soil and topographic properties. *Journal of Hydrology*, 53(3-4), 229–246. (ISBN: 0022-1694) doi: 10.1016/0022-1694(81)90003-2
- pandas development team, T. (2020). *pandas-dev/pandas: Pandas*. Zenodo. doi: 10.5281/zenodo.3509134
- Pazzaglia, F. J. (2003). Landscape evolution models. In *Developments in Quaternary Sciences* (Vol. 1, pp. 247–274). Elsevier. doi: 10.1016/S1571-0866(03)01012-1
- Pelletier, J. D. (2013). 2.3 Fundamental Principles and Techniques of Landscape Evolution Modeling. In J. F. Shroder (Ed.), *Treatise on Geomorphology* (pp. 29–43). San Diego: Academic Press. doi: 10.1016/B978-0-12-374739-6.00025-7
- Perron, J. T., Dietrich, W. E., & Kirchner, J. W. (2008). Controls on the spacing of first-order valleys. *Journal of Geophysical Research: Earth Surface*, 113(4), 1–21. doi: 10.1029/2007JF000977
- Prancevic, J. P., & Kirchner, J. W. (2019). Topographic controls on the extension and retraction of flowing streams. *Geophysical Research Letters*, 0(0). doi: 10.1029/2018GL081799
- Riebe, C. S., Hahm, W. J., & Brantley, S. L. (2017). Controls on deep critical zone architecture: a historical review and four testable hypotheses. *Earth Surface Processes and Landforms*, 42(1), 128–156. doi: 10.1002/esp.4052
- Roering, J. J. (2008). How well can hillslope evolution models "explain" topography? Simulating soil transport and production with high-resolution topographic data. *Geological Society of America Bulletin*, 120(9-10), 1248–1262. doi: 10.1130/B26283.1
- Roering, J. J., Kirchner, J. W., & Dietrich, W. E. (1999). Evidence for nonlinear, diffusive sediment transport on hillslopes and implications for landscape morphology. *Water Resources Research*, 35(3), 853–870. doi: 10.1029/1998WR900090
- Roering, J. J., Kirchner, J. W., & Dietrich, W. E. (2001). Hillslope evolution by nonlinear, slope-dependent transport: Steady state morphology and equilibrium adjustment timescales. *Journal of Geophysical Research: Solid Earth*, 106(B8), 16499–16513. (Publisher: John Wiley & Sons, Ltd) doi: 10.1029/2001JB000323
- Rosenbloom, N. A., & Anderson, R. S. (1994). Hillslope and channel evolution in a marine terraced landscape, Santa Cruz, California. *Journal of Geophysical Research: Solid Earth*, 99(B7), 14013–14029. doi: 10.1029/94JB00048@10.1002/(ISSN)2169-9356.TECTOP1
- Sangireddy, H., Carothers, R. A., Stark, C. P., & Passalacqua, P. (2016). Controls of climate, topography, vegetation, and lithology on drainage density extracted from high resolution topography data. *Journal of Hydrology*, 537, 271–282. doi: 10.1016/j.jhydrol.2016.02.051
- Snyder, N. P., Whipple, K. X., Tucker, G. E., & Merritts, D. J. (2003). Channel response to tectonic forcing: field analysis of stream morphology and hydrology in the Mendocino triple junction region, northern California. *Geomorphology*, 53(1), 97–127. doi: 10.1016/S0169-555X(02)00349-5
- Tarboton, D. G., Bras, R. L., & Rodriguez-Iturbe, I. (1989). Scaling and elevation in river networks. *Water Resources Research*, 25(9), 2037–2051. (Publisher: John Wiley & Sons, Ltd) doi: 10.1029/WR025i009p02037
- Temme, A. J. A. M., Schoorl, J. M., Claessens, L., & Veldkamp, A. (2013). 2.13

- 1440 Quantitative Modeling of Landscape Evolution. In J. F. Shroder (Ed.), *Treatise on Geomorphology* (pp. 180–200). San Diego: Academic Press. doi: 10
 1441 .1016/B978-0-12-374739-6.00039-7
- 1442 Theodoratos, N., & Kirchner, J. W. (2020a). Dimensional analysis of a landscape
 1443 evolution model with incision threshold. *Earth Surface Dynamics*, 8(2), 505–
 1444 526. (Publisher: Copernicus GmbH) doi: <https://doi.org/10.5194/esurf-8-505-2020>
- 1445 Theodoratos, N., & Kirchner, J. W. (2020b). Graphically interpreting how incision
 1446 thresholds influence topographic and scaling properties of modeled landscapes.
 1447 *Earth Surface Dynamics Discussions*, 1–25. (Publisher: Copernicus GmbH)
 1448 doi: 10.5194/esurf-2020-45
- 1449 Theodoratos, N., Seybold, H., & Kirchner, J. W. (2018). Scaling and similarity
 1450 of a stream-power incision and linear diffusion landscape evolution model.
 1451 *Earth Surface Dynamics*, 6(3), 779–808. (Publisher: Copernicus GmbH) doi:
 1452 <https://doi.org/10.5194/esurf-6-779-2018>
- 1453 Tramblay, Y., Bouvier, C., Martin, C., Didon-Lescot, J.-F., Todorovik, D., & Domer-
 1454 gue, J.-M. (2010). Assessment of initial soil moisture conditions for event-
 1455 based rainfallrunoff modelling. *Journal of Hydrology*, 387(3), 176–187. doi:
 1456 10.1016/j.jhydrol.2010.04.006
- 1457 Troch, P. A., Lahmers, T., Meira, A., Mukherjee, R., Pedersen, J. W., Roy, T., &
 1458 Valdes-Pineda, R. (2015). Catchment coevolution: A useful framework for
 1459 improving predictions of hydrological change? *Water Resources Research*,
 1460 51(7), 4903–4922. (arXiv: 10.1002/2014WR016527 ISBN: 6176273099) doi:
 1461 10.1002/2015WR017032
- 1462 Troch, P. A., Paniconi, C., & Van Loon, E. E. (2003). Hillslope-storage Boussinesq
 1463 model for subsurface flow and variable source areas along complex hillslopes:
 1464 1. Formulation and characteristic response. *Water Resources Research*, 39(11).
 1465 doi: 10.1029/2002WR001728
- 1466 Tsujimoto, T. (1999). Sediment transport processes and channel incision: mixed
 1467 size sediment transport, degradation and armoring. In S. E. Darby & A. Simon
 1468 (Eds.), *Incised river channels: processes, forms, engineering, and management*
 1469 (pp. 37–66). Chichester ; New York: J. Wiley.
- 1470 Tucker, G. E. (2004). Drainage basin sensitivity to tectonic and climatic forcing:
 1471 implications of a stochastic model for the role of entrainment and erosion
 1472 thresholds. *Earth Surface Processes and Landforms*, 29(2), 185–205. doi:
 1473 10.1002/esp.1020
- 1474 Tucker, G. E., & Bras, R. L. (1998). Hillslope processes, drainage density, and land-
 1475 scape morphology. *Water Resources Research*, 34(10), 2751–2764. Retrieved
 1476 from <http://doi.wiley.com/10.1029/98WR01474> doi: 10.1029/98WR01474
- 1477 Tucker, G. E., Catani, F., Rinaldo, A., & Bras, R. L. (2001). Statistical analysis
 1478 of drainage density from digital terrain data. *Geomorphology*, 36(3), 187–202.
 1479 doi: 10.1016/S0169-555X(00)00056-8
- 1480 Tucker, G. E., & Slingerland, R. (1997). Drainage basin responses to climate change.
 1481 *Water Resources Research*, 33(8), 2031–2047. doi: 10.1029/97WR00409
- 1482 Valters, D. (2016). Modelling Geomorphic Systems: Landscape Evolution. In
 1483 (p. 6.5.12). doi: 10.13140/RG.2.1.1970.9047
- 1484 West, A. J., Galy, A., & Bickle, M. (2005). Tectonic and climatic controls on silicate
 1485 weathering. *Earth and Planetary Science Letters*, 235(1), 211–228. doi:
 1486 10.1016/j.epsl.2005.03.020
- 1487 Whipple, K. X. (2001). Fluvial Landscape Response Time: How Plausible Is Steady-
 1488 State Denudation? *American Journal of Science*, 301(4–5), 313–325. (Pub-
 1489 lisher: American Journal of Science) doi: 10.2475/ajs.301.4-5.313
- 1490 Whipple, K. X., Hancock, G. S., & Anderson, R. S. (2000, 03). River incision into
 1491 bedrock: Mechanics and relative efficacy of plucking, abrasion, and cavita-
 1492 tion. *GSA Bulletin*, 112(3), 490–503. doi: 10.1130/0016-7606(2000)112<490:
- 1493

- RIIBMA)2.0.CO;2
- Whipple, K. X., & Tucker, G. E. (1999). Dynamics of the stream-power river incision model: Implications for height limits of mountain ranges, landscape response timescales, and research needs. *Journal of Geophysical Research: Solid Earth*, *104*(B8), 17661–17674. doi: 10.1029/1999JB900120
- Willgoose, G., Bras, R. L., & Rodriguez-Iturbe, I. (1991). A coupled channel network growth and hillslope evolution model: 1. Theory. *Water Resources Research*, *1671*–1684. doi: 10.1029/91WR00935@10.1002/(ISSN)1944-7973.USALPINE1
- Willgoose, G., Bras, R. L., & Rodriguez-Iturbe, I. (1991a). A coupled channel network growth and hillslope evolution model: 2. Nondimensionalization and applications. *Water Resources Research*, *27*(7), 1685–1696. doi: 10.1029/91WR00936
- Willgoose, G., Bras, R. L., & Rodriguez-Iturbe, I. (1991b). A physical explanation of an observed link area-slope relationship. *Water Resources Research*, *27*(7), 1697–1702. (Publisher: John Wiley & Sons, Ltd) doi: 10.1029/91WR00937
- Wohl, E., & David, G. C. L. (2008). Consistency of scaling relations among bedrock and alluvial channels. *Journal of Geophysical Research: Earth Surface*, *113*(F4). doi: <https://doi.org/10.1029/2008JF000989>
- Yoshida, T., & Troch, P. A. (2016). Coevolution of volcanic catchments in Japan. *Hydrology and Earth System Sciences*, *20*(3), 1133–1150. (ISBN: 1607-7938) doi: 10.5194/hess-20-1133-2016
- Zhang, Y., Slingerland, R., & Duffy, C. (2016). Fully-coupled hydrologic processes for modeling landscape evolution. *Environmental Modelling and Software*, *82*, 89–107. doi: 10.1016/j.envsoft.2016.04.014